

December 2, 2024

LBNL-41826
hep-ph/9805402

Radiative Decay of a Long-Lived Particle and Big-Bang Nucleosynthesis*

Erich Holtmann^a, M. Kawasaki^b, K. Kohri^b, and Takeo Moroi^a

^a *Theoretical Physics Group, Ernest Orlando Lawrence Berkeley National Laboratory, University of California, Berkeley, California 94720*

^b *Institute for Cosmic Ray Research, The University of Tokyo, Tanashi 188-8502, Japan*

Abstract

The effects of radiatively decaying, long-lived particles on big-bang nucleosynthesis (BBN) are discussed. If high energy photons are emitted after BBN, they may change the abundances of the light elements through photodissociation processes, which may result in a significant discrepancy between the BBN theory and observation. We calculate the abundances of the light elements, including the effects of photodissociation induced by a radiatively decaying particle, and we derive a constraint on such particles by comparing our theoretical results with observations. Taking into account the recent controversies regarding the observations of the primordial D and ^4He abundances, we derive constraints for various combinations of the measurements. We also discuss several models which predict such radiatively decaying particles, and we derive constraints on such models.

* This work was supported by the Director, Office of Energy Research, Office of Basic Energy Services, of the U.S. Department of Energy under Contract DE-AC03-76SF00098. K.K. is supported by JSPS Research Fellowship for Young Scientists.

1 Introduction

Big-bang nucleosynthesis (BBN) has been used to impose constraints on neutrinos and other hypothetical particles predicted by particle physics, because BBN is very sensitive to the thermal history of the early universe at temperatures $T \lesssim 1$ MeV [1].

Weakly interacting massive particles appear often in particle physics. In this paper, we consider particles which have masses of $\sim O(100$ GeV) and which interact with other particle only very weakly (*e.g.*, through gravitation). These particles have lifetimes so long that they decay after the BBN of the light elements (D, 3 He, 4 He, etc.), so they and their decay products may affect the thermal history of the universe. In particular, if the long-lived particles decay into photons, then the emitted high energy photons induce electro-magnetic cascades and produce many soft photons. If the energy of these photons exceeds the binding energies of the light nuclides, then photodissociation may profoundly alter the light element abundances. Thus, we can impose constraints on the abundance and lifetime of long-lived particles, by considering the photodissociation processes induced by its decay. There are many works on this subject, such as the constraints on massive neutrinos and gravitinos obtained by the comparison between the theoretical predictions and observations [2, 3, 4, 5, 6].

A couple of years ago, Hata *et al.* [7] claimed that light-element observations seemed to conflict with the theoretical predictions of standard BBN. Their point was that standard BBN predicts too much 4 He, if the baryon number density is determined by the D abundance inferred from observations; equivalently, standard BBN predicts too much D, if the baryon number density is determined by the 4 He observations. Inspired by this “crisis in BBN,” many people re-examined standard and non-standard BBN by including systematic errors in the observations, or by introducing some non-standard properties of neutrinos [8, 9]. In a previous paper [10], we investigated the effect upon BBN of radiatively-decaying massive particles. These particles induce an electro-magnetic cascade. We found that in a certain parameter region, the photons in this cascade destroy only D, so that the predicted abundances of D, 3 He, and 4 He fit the observations.

However, since the “BBN crisis” was claimed, the situation concerning the observations of the light elements has changed. First, the D abundances in highly red-shifted quasar absorption systems (QAS) have been observed by two groups. The abundance of D in high- z QAS is considered to be the primordial value. Thanks to these direct new observations, we no longer need to use poorly-understood models of chemical evolution to infer the primordial abundance from the material in solar neighborhood. Unfortunately, however, the D abundance measured by the first group [11, 12, 13] is not consistent with the abundance measured by the other [14]. We may have to wait for more data before we can decide the primordial abundance of D.

Second, the observations of 4 He have also changed. For a long time, the relatively low 4 He abundance (*viz.*, $Y \simeq 0.234$, where Y is the primordial mass fraction of 4 He) [15, 16] was believed. Recently, however, a higher 4 He abundance ($Y \simeq 0.244$) has been reported [17, 18]. The typical errors in 4 He observations are less than $\simeq 0.005$, so we have

discordant data for ${}^4\text{He}$ as well as for D.

Since we have new observations for D and ${}^4\text{He}$, the previous constraint on the radiative decay of long-lived particles must be revised. In addition, the statistical analyses on radiatively decaying particles are insufficient in the previous works. Therefore, in our present paper, we perform a better statistical analysis of a long-lived, radiatively-decaying particle, and of the resultant photodissociations, in order to constrain the abundances and lifetimes of long-lived particles. In deriving the constraint, we use all four combinations of the observed abundances of D and ${}^4\text{He}$, because it is premature to decide which data are correct. As a result, it will be shown that for a certain combination of the observed data, we have a discrepancy between observations and standard BBN theory. Moreover, we show in that case that a long-lived particle with appropriate abundance and lifetime can solve the discrepancy. In the other cases, standard BBN fits the observations, so we derive stringent constraints on the properties of long-lived particles.

In this paper, we also include the photodissociations of ${}^7\text{Li}$ and ${}^6\text{Li}$ for the first time. As we will show later, the destruction of ${}^7\text{Li}$ does not dramatically affect the predicted D and ${}^4\text{He}$, in the region where the observed D and ${}^4\text{He}$ values are best fit. However, the ${}^6\text{Li}$ produced by the destruction of ${}^7\text{Li}$ can be two orders of magnitude more abundant than the standard BBN prediction of ${}^6\text{Li}/\text{H} \sim O(10^{-12})$. We discuss the possibility that this process may be the origin of the ${}^6\text{Li}$ which is observed in some low-metallicity halo stars.

In Sec. 2 we study how consistent the theoretically predicted abundances and observations are, in the case of standard BBN. The radiative decay of long-lived particles is considered in Sec. 3, and the particle physics models which predict such long-lived particles are presented in Sec. 4. Finally, Sec. 5 is devoted to discussion and the conclusion.

2 Standard Big-Bang Nucleosynthesis

We begin by reviewing standard big-bang nucleosynthesis (SBBN). We are interested in the light elements, since their primordial abundances can be estimated from observations. In particular, we check the consistency between the theoretical predictions and the observations for the following quantities:

$$y_2 = n_{\text{D}}/n_{\text{H}}, \quad (1)$$

$$Y = \rho_{{}^4\text{He}}/\rho_{\text{B}}, \quad (2)$$

$$y_6 = n_{{}^6\text{Li}}/n_{\text{H}}, \quad (3)$$

$$y_7 = n_{{}^7\text{Li}}/n_{\text{H}}. \quad (4)$$

where ρ_{B} is the total baryon energy density. Notice that we do not discuss ${}^3\text{He}$, since we would have to use a poorly-understood model of chemical evolution if we were to estimate its primordial abundance. However, even without ${}^3\text{He}$, we obtain a non-trivial constraint on the BBN model, as we will show below.

In this section, we first review the observations of the light elements, and the extrapolations back to the primordial abundances. Next, we describe our theoretical calculations of these abundances, by using standard big-bang theory as an example. Finally, we compare the theoretical and observed light-element abundances to determine how well the SBBN theory works.

2.1 Review of Observation

Let us start with a review of the observations of the light element abundances. Two factors complicate the interpretation of the observations of the light-element abundances. First, there are several observational results (both for D/H and for ^4He) which are not consistent with each other, within the quoted errors. This fact suggests that some groups have underestimated their systematic error.¹ We believe it is premature to judge which measurements are reliable; hence, we consider all possible combinations of the observations when we test the consistency between theory and observation. Second, some guesswork is involved in the extrapolation back from the observed values to the primordial values, as we shall discuss below. Keeping these factors in mind, we review the estimations of the primordial abundances of D, ^4He , ^6Li , and ^7Li .

D/H has been measured in the absorption lines of highly red-shifted (and therefore presumably primordial) H_I (neutral hydrogen) clouds which are backlit by quasars. However, the D/H measurements from these QAS generally fall into two classes, viz., high and low, which differ by almost an order of magnitude.

The first three measurements (all in the direction of QSO 0014+813) were high [11, 20, 13], in the range $y_2 = (1.9 - 2.5) \times 10^{-4}$. Since these original observations, there have been additional measurements [12, 21] of high D/H in this and other QAS. However, Carswell *et al.* state that there is a significant probability that their “deuterium” may actually be Doppler-shifted hydrogen [20] in an interloping H_I cloud. Steigman [22] claims that this may be the case in other measurements, as well, although Rutgers and Hogan [13] say that an interloper is very unlikely. Finally, Tytler, Burles, and Kirkman [23] reobserved QSO 0014+813 and found that their higher-quality data yield a very large uncertainty in D/H.

On the other hand, Tytler *et al.* [24] have found much smaller values of D/H, viz. $y_2 \sim 2.4 \pm 0.4$, in the directions of QAS 1937-1009 and QAS 1009-2956. However, a reanalysis [25] of Tytler’s QAS 1937-1009 data yields a much higher D/H value. Similarly, new data for QSO 1937-1009 [26] also yields higher D/H.

Because of these conflicting measurements, we will perform several analyses in our paper. For our low values, we use the recent determination of Burles and Tytler [14]. This value is slightly higher than their original measurement, because they use an improved model of the cloud and have a better measurement of the neutral hydrogen:

$$\text{Low: } y_2^{\text{obs}} = (3.39 \pm 0.25) \times 10^{-5}. \quad (5)$$

¹We do not believe that the discordant measured abundances are evidence of inhomogeneity, because such a large-scale primordial inhomogeneity is ruled out by the observed smoothness of the cosmic microwave background [19].

We take our high value from Rutgers and Hogan [13]:

$$\text{High: } y_2^{\text{obs}} = (1.9 \pm 0.5) \times 10^{-4}. \quad (6)$$

In this paper, we do not rely upon the presolar and interstellar-medium measurements of D and ^3He , because of the uncertainty involved in extrapolating back to the primordial abundance of D/H. An analysis based upon these measurements will appear in a separate paper by one of the authors (E.H.). This analysis generally agrees with the low QAS D/H in this paper.

The primordial ^4He abundance is deduced from observations of extragalactic H_{II} regions (clouds of ionized hydrogen). Currently, there are two classes of Y^{obs} , reported by several independent groups of observers. Hence, we consider two cases: one low, and one high.

We take our low ^4He abundance from Olive, Skillman, and Steigman [16]. They used measurements of ^4He and O/H in 62 extragalactic H_{II} regions, and linearly extrapolated back to O/H = 0 to deduce the primordial value

$$\text{Low: } Y^{\text{obs}} = 0.234 \pm (0.002)_{\text{stat}} \pm (0.005)_{\text{syst}}. \quad (7)$$

(When they restrict their data set to only the lowest metallicity data, they obtain $Y^{\text{obs}} = 0.230 \pm 0.003$.) Their systematic error comes from numerous sources, but they claim that no source expected to be much more than 2%. In particular, they estimate that stellar absorption is of order 1% or less.

We take our high ^4He abundance from Thuan and Izotov [17]. They used measurements of ^4He and O/H in a new sample of 45 blue compact dwarf galaxies to obtain

$$\text{High: } Y^{\text{obs}} = 0.244 \pm (0.002)_{\text{stat}} \pm (0.005)_{\text{syst}}. \quad (8)$$

The last error is an estimate of the systematic error, taken from Izotov, Thuan, and Lipovetsky [18]. Thuan and Izotov claim that HeI stellar absorption is an important effect; this explains some of the difference between their result and that of Olive, Skillman, and Steigman.

Rather than attempting to judge which group has done a better job of choosing their sample and correcting for systematic errors, we prefer to remain open-minded. Hence, we shall use both the high and low ^4He abundances, without expressing a preference for one over the other.

The $^7\text{Li}/\text{H}$ abundance is taken from observations of the surfaces of Pop II (old) halo stars. In general, Li/H decreases with decreasing stellar surface temperature, since cooler (*i.e.*, lower mass) stars have deeper convection zones, and ^7Li is destroyed in the warm interior of a star. However, Spite and Spite [27] found that at high surface temperatures, $^7\text{Li}/\text{H}$ levels off into a “plateau.” This is interpreted as the primordial value of y_7 . Similarly, it was found that ^7Li decreases with decreasing Fe/H (iron indicates non-primordial matter), but ^7Li levels off at very low metallicities ($[\text{Fe}/\text{H}] \leq -1.5$).² Using

² $[\text{Fe}/\text{H}] \equiv \log_{10}(n_{\text{Fe}}/n_{\text{H}}) - \log_{10}(n_{\text{Fe}}/n_{\text{H}})_{\text{presolar}}$.

data from 41 plateau stars, Bonifacio and Molaro [28] determine the primordial value $\log_{10}(y_7^{obs}) = -9.762 \pm (0.012)_{stat} \pm (0.05)_{syst}$. Bonifacio and Molaro argue that the data provides no evidence for ${}^7\text{Li}/\text{H}$ depletion in the stellar atmospheres (caused by, *e.g.*, stellar winds, rotational mixing, or diffusion). However, for our analysis, we shall adopt the more cautious estimate of Hogan [29] that ${}^7\text{Li}$ may have been supplemented (by production in cosmic-ray interactions) or depleted (in stars) by a factor of two: [30]

$$\log_{10}(y_7^{obs}) = -9.76 \pm (0.012)_{stat} \pm (0.05)_{syst} \pm (0.3)_{\text{factor of 2}}. \quad (9)$$

Because ${}^6\text{Li}$ is so much rarer than ${}^7\text{Li}$, it is much more difficult to observe. Currently, there is insufficient data to find the “Spite plateau” of ${}^6\text{Li}$. However, we can set an upper bound on ${}^6\text{Li}/{}^7\text{Li}$, since it is generally agreed that the evolution of ${}^6\text{Li}$ is dominated by production by spallation (reactions of cosmic rays with the interstellar medium). The upper bounds on ${}^6\text{Li}/{}^7\text{Li}$ observed in low-metallicity ($[\text{Fe}/\text{H}] \leq -2.0$) halo stars range from [31] $y_6/y_7 \lesssim 0.045$ to $y_6/y_7 \lesssim 0.13$. (Note that the primordial ${}^6\text{Li}$ and ${}^7\text{Li}$ have both been destroyed in material which has been processed by stars.)

Rotational mixing models [32] yield a survival factor for ${}^7\text{Li}$ of order 0.05 and a survival factor for ${}^6\text{Li}$ of order 0.005. Therefore, the upper bound for primordial ${}^6\text{Li}/{}^7\text{Li}$ ranges approximately from

$$y_6^{obs}/y_7^{obs} \lesssim 0.5 \text{ to } 1.3. \quad (10)$$

Since we have only a rough range of upper bounds on ${}^6\text{Li}$, and no lower bound, we will not use ${}^6\text{Li}$ in our statistical analysis to test the concordance between observation and theory. Instead, we will just check the consistency of our theoretical results with the above constraint.

2.2 Theoretical Calculations

Theoretically, the primordial abundances of the light elements in SBBN depend only upon a single parameter: the baryon-to-photon ratio η . In our analysis, we modified Kawano’s nucleosynthesis code [33] to calculate the primordial light-element abundances and uncertainties.

In our calculation, we included the uncertainty in the neutron lifetime [34] and in the 11 most important nuclear reaction rates [35]. We treated the neutron lifetime and the nuclear reaction rates as independent random variables with Gaussian probability density functions (p.d.f.’s). We performed a Monte-Carlo over the neutron lifetime and the 11 nuclear reaction rates, and we found that the light-element abundances were distributed approximately according to independent, Gaussian p.d.f.’s. Therefore, the p.d.f. p_{tot}^{th} for the theoretical abundances is given by the product of the Gaussian p.d.f.’s

$$p^{Gauss}(x; \bar{x}, \sigma) = \frac{1}{\sqrt{2\pi}\sigma} \exp \left[-\frac{1}{2} \left(\frac{x - \bar{x}}{\sigma} \right)^2 \right] \quad (11)$$

for the individual light elements:

$$p_{tot}^{th}(y_2^{th}, Y^{th}, \log_{10} y_7^{th}) = p_2^{Gauss}(y_2^{th}) \times p_4^{Gauss}(Y^{th}) \times p_7^{Gauss}(\log_{10} y_7^{th}). \quad (12)$$

In Fig. 1, we have plotted the theoretical predictions for the light-element abundances (solid lines) with their one-sigma errors (dashed lines), as functions of η .

The dependences of the abundances on η can be seen intuitively[1, 36]. The ${}^4\text{He}$ abundance is a gentle, monotonically increasing function of η . As η increases, ${}^4\text{He}$ is produced earlier because the “deuterium bottleneck” is overcome at a higher temperature due to the higher baryon density. Fewer neutrons have had time to decay, so more ${}^4\text{He}$ is synthesized. Since ${}^4\text{He}$ is the most tightly bound of the light nuclei, D and ${}^3\text{He}$ are fused into ${}^4\text{He}$. The surviving abundances of D and ${}^3\text{He}$ are determined by the competition between their destruction rates and the expansion rate. The destruction rates are proportional to η , so the larger η is, the longer the destruction reactions continue. Therefore, D and ${}^3\text{He}$ are monotonically decreasing functions of η . Moreover, the slope of D is steeper, because the binding energy of D is smaller than ${}^3\text{He}$.

The graph of ${}^7\text{Li}$ has a “trough” near $\eta \sim 3 \times 10^{-10}$. For a low baryon density $\eta \lesssim 3 \times 10^{-10}$, ${}^7\text{Li}$ is produced by ${}^4\text{He}(T, \gamma){}^7\text{Li}$ and is destroyed by ${}^7\text{Li}(p, \alpha){}^4\text{He}$. As η increases, the destruction reaction becomes more efficient and the produced ${}^7\text{Li}$ tends to decrease. On the other hand for a high baryon density $\eta \gtrsim 3 \times 10^{-10}$, ${}^7\text{Li}$ is mainly produced through the electron capture of ${}^7\text{Be}$, which is produced by ${}^3\text{He}(\alpha, \gamma){}^7\text{Be}$. Because ${}^7\text{Be}$ production becomes more effective as η increases, the synthesized ${}^7\text{Li}$ increases. The “trough” results from the overlap of these two components. The dominant source of ${}^6\text{Li}$ in SBBN is $D(\alpha, \gamma){}^6\text{Li}$. Thus, the η dependence of ${}^6\text{Li}$ resembles that of D.

We have also plotted the 1- σ observational constraints. The amount of overlap of the boxes is a rough measure of the consistency between theory and observations. We can also see the favored ranges of η . However, we will discuss the details of our analysis more carefully in the following section.

2.3 Statistical Analysis and Results

Next, let us briefly explain how we quantify the consistency between theory and observation. For this purpose, we define the variable χ^2 as

$$\chi^2 = \sum_i \frac{(a_i^{th} - a_i^{obs})^2}{(\sigma_i^{th})^2 + (\sigma_i^{obs})^2} \quad (13)$$

where $a_i = (y_2, Y, \log_{10} y_7)$, and we add the systematic errors in quadrature: $(\sigma_i^{obs})^2 = (\sigma_i^{syst})^2 + (\sigma_i^{stat})^2$. (See Appendix A for a detailed explanation of our use of χ^2 .) χ^2 depends upon the parameters of our theory (viz. η in SBBN) through a_i^{th} and σ_i^{th} .

Notice that we do not include ${}^6\text{Li}$ in the calculation of χ^2 , since the ${}^6\text{Li}$ abundance has not been measured well. Instead, we check that y_6^{th}/y_7^{th} satisfies the bound (10). In the case of SBBN, we found that the ${}^6\text{Li}$ abundance is small enough over the entire range

	N_ν (95 % C.L.)	$\eta \times 10^{10}$ (95 % C.L.)
Low ^4He & Low D	$2.1^{+1.0}_{-0.8}$	$4.7^{+1.0}_{-0.8}$
Low ^4He & High D	$3.0^{+1.2}_{-1.1}$	$1.8^{+1.9}_{-0.5}$
High ^4He & Low D	$2.8^{+1.0}_{-1.0}$	$5.0^{+1.0}_{-0.8}$
High ^4He & High D	$3.7^{+1.3}_{-1.2}$	$1.9^{+2.1}_{-0.6}$

Table 1: Observational constraints on η and N_ν in SBBN

of η from 8.0×10^{-11} to 1.0×10^{-9} . (Numerically, $y_6^{th}/y_7^{th} < 5 \times 10^{-4}$, which is well below the bound (10).)

With this χ^2 variable, we discuss how well the theoretical prediction agrees with observation. More precisely, we calculate from χ^2 the confidence level (C.L.) with which the SBBN theory is excluded, at a given point in the parameter space of our theory (for three degrees of freedom):

$$\text{C.L.} = \int_0^{\chi^2} \frac{1}{2^{3/2}\Gamma(\frac{3}{2})} y^{\frac{1}{2}} e^{-\frac{y}{2}} dy \quad (14)$$

$$= -\sqrt{\frac{2\chi^2}{\pi}} \exp\left(-\frac{\chi^2}{2}\right) + \text{erf}\left(\sqrt{\frac{\chi^2}{2}}\right), \quad (15)$$

In Fig. 2, we have plotted the χ^2 and confidence level at which SBBN theory is excluded by the observations, as a function of η . We find that high D is allowed at better than the 68% C.L. at $\eta \sim 2 \times 10^{-10}$, while low D and high ^4He is allowed at better than the 68% C.L. at $\eta \sim 5 \times 10^{-10}$. However, for low D and low ^4He , no value of eta works at the 91.5% C.L.

The case of low ^4He and low D suggests a discrepancy with standard BBN. Some people believe that this casts doubt on the low D or low ^4He measurements[37]. However, we do not want to assume SBBN theory and use it to judge the validity of the observations; rather, we use the observations to test BBN theory. Therefore, we give equal consideration to all four combinations of the observed abundances.

Before closing this section, we apply our analysis to constrain the number of neutrino species. Here, we vary η and the number N_ν of neutrino species, and we calculate the confidence level as a function of these variables. The results are shown in Fig. 3a,b for four combinations of the observations. We can see that the standard scenario ($N_\nu = 3$) results in a good fit, except for the case of low D and low ^4He . In fact, low D and low ^4He prefers $N_\nu \sim 2$, as pointed out by [7, 9]. However, for the other combinations, $N_\nu = 3$ is completely consistent with observation. In Table 1, we show the 95% C.L. bounds for the number of neutrino species N_ν and η in the four cases.

3 BBN + X

In this section, we discuss the implications of a radiatively decaying particle X for BBN. For this purpose, we first discuss the behavior of the photon spectrum induced by X . Then we show the abundances of the light elements, including the effects of the photodissociation induced by X . Comparing these abundances with observations, we constrain the parameter space for η and X .

3.1 Photon spectrum

In order to discuss the effect of high-energy photons on BBN, we need to know the shape of the photon spectrum induced by the primary high-energy photons from X decay.

In the background thermal bath (which, in our case, is a mixture of photons γ_{BG} , electrons e_{BG}^- , and nucleons N_{BG}), high energy photons lose their energy by various cascade processes. In the cascade, the photon spectrum is induced, as discussed in various literature[38]. The important processes in our case are:

- Double-photon pair creation ($\gamma + \gamma_{\text{BG}} \rightarrow e^+ + e^-$)
- Photon-photon scattering ($\gamma + \gamma_{\text{BG}} \rightarrow \gamma + \gamma$)
- Pair creation in nuclei ($\gamma + N_{\text{BG}} \rightarrow e^+ + e^- + N$)
- Compton scattering ($\gamma + e_{\text{BG}}^- \rightarrow \gamma + e^-$)
- Inverse Compton scattering ($e^\pm + \gamma_{\text{BG}} \rightarrow e^\pm + \gamma$)

(We may neglect double Compton scattering $\gamma + e_{\text{BG}}^- \rightleftharpoons \gamma + \gamma + e^-$, because Compton scattering is more important for thermalizing high-energy photons.) In our analysis, we numerically solved the Boltzmann equation including the above effects, and obtained the distribution function of photons, $f_\gamma(E_\gamma)$. (For details, see Refs. [4, 5].)

In Fig. 4, we show the photon spectrum for several temperatures T . Roughly speaking, we can see a large dropoff at $E_\gamma \sim m_e^2/22T$ for each temperature. Above this threshold, the photon spectrum is extremely suppressed.

The qualitative behavior of the photon spectrum can be understood in the following way. If the photon energy is high enough, then double-photon pair creation is so efficient that this process dominates the cascade. However, once the photon energy becomes much smaller than $O(m_e^2/T)$, this process is kinematically blocked. Numerically, this threshold is about $m_e^2/22T$, as we mentioned. Then, photon-photon scattering dominates. However, since the scattering rate due to this process is proportional to E_γ^3 , photon-photon scattering becomes unimportant in the limit $E_\gamma \rightarrow 0$. Therefore, for $E_\gamma \ll O(m_e^2/T)$, the remaining processes (pair creation in nuclei and inverse Compton scattering) are the most important.

The crucial point is that the scattering rate for $E_\gamma \gtrsim m_e^2/22T$ is much larger than that for $E_\gamma \ll m_e^2/22T$, since the number of targets in the former case is several orders of magnitude larger than in the latter. This is why the photon spectrum is extremely suppressed for $E_\gamma \gtrsim m_e^2/22T$. As a result, if the X particle decays in a thermal bath with temperature $T \gtrsim m_e^2/22Q$ (where Q is the binding energy of a nuclide) then photodissociation is not effective.

3.2 Abundance of light elements with X

Once the photon spectrum is formed, it induces the photodissociation of the light nuclei, which modifies the result of SBBN. This process is governed by the following Boltzmann equation:

$$\frac{dn_N}{dt} + 3Hn_N = \left[\frac{dn_N}{dt} \right]_{\text{SBBN}} - n_N \sum_{N'} \int dE_\gamma \sigma_{N\gamma \rightarrow N'}(E_\gamma) f_\gamma(E_\gamma) + \sum_{N''} n_{N''} \int dE_\gamma \sigma_{N''\gamma \rightarrow N}(E_\gamma) f_\gamma(E_\gamma), \quad (16)$$

where n_N is the number density of the nuclei N , and $[dn_N/dt]_{\text{SBBN}}$ denotes the SBBN contribution to the Boltzmann equation. To take account of the photodissociation processes, we modified the Kawano code [33], and calculated the abundances of the light elements. The photodissociation processes we included in our calculation are listed in Table 2.

The abundances of light nuclides will be functions of the lifetime of X (τ_X), the mass of X (m_X), the abundance of X before electron-positron annihilation

$$Y_X = n_X/n_\gamma, \quad (17)$$

and the baryon-to-photon ratio (η). In our numerical BBN simulations, we found that the nuclide abundances depend only on the mass abundance $m_X Y_X$, not on m_X and Y_X separately. In Figs. 5 – 8, we show the abundances of light nuclei in the $m_X Y_X$ vs. τ_X plane, at fixed η .

We can understand the qualitative behaviors of the abundances in the following way. First of all, if the mass density of X is small enough, then the effects of X are negligible, and hence we reproduce the result of SBBN. Once the mass density gets larger, the SBBN results are modified. The effects of X strongly depend on τ_X , the lifetime of X . As we mentioned in the previous section, photons with energy greater than $\sim m_e^2/22T$ participate in pair creation before they can induce photofission. Therefore, if the above threshold energy is smaller than the nuclear binding energy, then photodissociation is not effective.

If $\tau_X \lesssim 10^4$ sec, then $m_e^2/22T \lesssim 2\text{MeV}$ at the decay time of X , and photodissociation is negligible for all elements. In this case, the main effect of X is on the ${}^4\text{He}$ abundances: if the abundance of X is large, its energy density speeds up the expansion rate of the universe, so the neutron freeze-out temperature becomes higher. As a result, ${}^4\text{He}$ abundance is enhanced relative to SBBN.

Photofission Reactions	1 σ Uncertainty	Threshold Energy	Ref.
1. $D + \gamma \rightarrow p + n$	6%	2.2 MeV	[39]
2. $T + \gamma \rightarrow n + D$	14%	6.3 MeV	[40, 41]
3. $T + \gamma \rightarrow p + 2n$	7%	8.5 MeV	[41]
4. $^3\text{He} + \gamma \rightarrow p + D$	10%	5.5 MeV	[42]
5. $^3\text{He} + \gamma \rightarrow n + 2p$	15%	7.7 MeV	[42]
6. $^4\text{He} + \gamma \rightarrow p + T$	4%	19.8 MeV	[42]
7. $^4\text{He} + \gamma \rightarrow n + ^3\text{He}$	5%	20.6 MeV	[43, 44]
8. $^4\text{He} + \gamma \rightarrow p + n + D$	14%	26.1 MeV	[45]
9. $^6\text{Li} + \gamma \rightarrow \text{anything}$	4%	5.7 MeV	[46]
10. $^7\text{Li} + \gamma \rightarrow 2n + \text{anything}$	9%	10.9 MeV	[46]
11. $^7\text{Li} + \gamma \rightarrow n + ^6\text{Li}$	4%	7.2 MeV	[46]
12. $^7\text{Li} + \gamma \rightarrow ^4\text{He} + \text{anything}$	9%	2.5 MeV	[46]
13. $^7\text{Be} + \gamma \rightarrow p + ^6\text{Li}$			
14. $^7\text{Be} + \gamma \rightarrow \text{anything except } ^6\text{Li}$			

Table 2: Photodissociation processes, and the 1- σ uncertainty in the cross sections. Since there is no experimental data on photodissociation of ^7Be , we assume in this paper that the rate for Reaction 13 is the same as for Reaction 11, and the rate for Reaction 14 is the sum of the rates for Reactions 10 and 12.

If $10^4 \text{ sec} \lesssim \tau_X \lesssim 10^6 \text{ sec}$, then $2 \text{ MeV} \lesssim m_e^2/22T \lesssim 20 \text{ MeV}$. In this case, ^4He remains intact, but D is effectively photodissociated through the process $D + \gamma \rightarrow p + n$.

If the lifetime is long enough ($\tau_X \gtrsim 10^6 \text{ sec}$), ^4He can be also effectively destroyed. In this case, the destruction of even a small fraction of the ^4He can result in significant production of D , since the ^4He abundance is originally much larger than that of D . This can be seen in Figs. 5 and 6: for $\tau_X \gtrsim 10^6 \text{ sec}$ and $10^{-10} \text{ GeV} \lesssim m_X Y_X \lesssim 10^{-9} \text{ GeV}$, the abundance of D changes drastically due to the photodissociation of ^4He . If $m_X Y_X$ is large enough, all the light elements are destroyed efficiently, resulting in very small abundances.

So far, we have discussed the theoretical calculation of the light element abundances in a model with X decay. In the next section, we compare the theoretical calculations with observations, and derive constraints on the properties of X .

3.3 Comparison with observation

As we mentioned in Section 2.1, we have two ^4He and two D values which are inferred from various observed data to be the primordial components. In this section we compare the theoretical calculations with these observed abundances and show how we can constrain the model parameters in each of the four cases.

3.3.1 Low ${}^4\text{He}$ ($Y^{obs} = 0.234 \pm (0.002)_{stat} \pm (0.005)_{syst}$)

Recalling that the low observed ${}^4\text{He}$ value [Eq. (7)] is consistent with the theoretical calculation at low η in the case of SBBN, we expect that we can obtain rigid constraints on the model parameters for the high observed D value [Eq. (6)]. On the other hand, for the low observed D value [Eq. (5)] we search the parameter space for regions of better fit than we can obtain with SBBN.

Low D ($y_2^{obs} = (3.39 \pm 0.25) \times 10^{-5}$)

In Fig. 9 we show the contours of the confidence level computed using three elements (D, ${}^4\text{He}$, and ${}^7\text{Li}$), for some representative η values ($\eta_{10} = 2, 4, 5, 6$), where

$$\eta_{10} \equiv \eta \times 10^{10}. \quad (18)$$

The region of parameter space which is allowed at the 68% C.L. extends down to low η (see Fig. 9a). Near $\eta_{10} = 2$, deuterium is destroyed by an order of magnitude (without net destruction of ${}^4\text{He}$), so that the remaining deuterium agrees with the calculated low ${}^4\text{He}$. We also plotted the regions excluded by the observational upper bounds on ${}^6\text{Li}/{}^7\text{Li}$. The shaded regions are $y_6/y_7 \gtrsim 0.5$, and the darker shaded regions are $y_6/y_7 \gtrsim 1.3$. Even if we adopt the stronger bound $y_6/y_7 \lesssim 0.5$, our theoretical results are consistent with the observed ${}^6\text{Li}$ value.

In Fig. 10, we show the contours of the confidence levels for various lifetimes, $\tau_X = 10^4, 10^5, 10^6$ sec. As the lifetime decreases, the background temperature at the time of decay increases, so the threshold energy of double-photon pair creation decreases. Then for a fixed $m_X Y_X$, the number of photons contributing to D destruction decreases. Thus, for shorter lifetimes, we need larger $m_X Y_X$ in order to destroy sufficient amounts of D. The observed abundances prefer nonvanishing $m_X Y_X$.

In Fig. 11, we show contours of χ^2 which have been projected along the η axis into the $\tau_X - m_X Y_X$ plane. By projection, we mean taking the lowest C.L. value along the η axis for a fixed point $(\tau_X, m_X Y_X)$.

The lower $m_X Y_X$ region, *i.e.* $m_X Y_X \sim 10^{-14}$ GeV, corresponds to SBBN, since there are not enough photons to affect the light element abundances. It is notable that these regions are outside of the 68% C.L. This fact may suggest the existence of a long-lived massive particle X and may be regarded as a hint of physics beyond the standard model or standard big bang cosmology.

For example, in Fig. 12 we show the predicted abundances of ${}^4\text{He}$, D, ${}^7\text{Li}$ and ${}^6\text{Li}$ adopting the model parameters $\tau_X = 10^6$ sec and $m_X Y_X = 5 \times 10^{10}$ GeV. The predicted abundances of ${}^4\text{He}$ and ${}^7\text{Li}$ are nearly the same as in SBBN. Only D is destroyed; its abundance decreases by about 80%. At low $\eta \sim (1.7 - 2.3) \times 10^{-10}$ in this model, the predicted abundances of these three elements agree with the observed values. It is interesting that the produced ${}^6\text{Li}$ abundance can be two orders of magnitude larger than the SBBN prediction in this parameter region. The origin of the observed ${}^6\text{Li}$ abundance,

$\tau_X = 10^4$ sec	10^5 sec	10^6 sec	10^7 sec	10^8 sec	10^9 sec
95% C.L. 9×10^{-6}	9×10^{-9}	1×10^{-9}	7×10^{-11}	2×10^{-12}	7×10^{-13}
68% C.L. $(1 - 9) \times 10^{-6}$	$(1 - 7) \times 10^{-9}$	$(2 - 9) \times 10^{-10}$			

Table 3: Upper or (upper – lower) bound on $m_X Y_X$ in units of GeV for the case of low ${}^4\text{He}$ and low D. Note that the C.L. is for 3 degrees of freedom, and η is varied to give the extreme values for $m_X Y_X$.

${}^6\text{Li}/\text{H} \sim O(10^{-12})$ is usually explained by cosmic ray spallation; however, our model demonstrates the possibility that ${}^6\text{Li}$ may have been produced by the photodissociation of ${}^7\text{Li}$ at an early epoch. Our ${}^6\text{Li}$ prediction is consistent with the upper bound Eq. (10).

Despite this, it is worth noting that SBBN lies within the 95% C.L. agreement between theory and observation. In Fig. 11 the 95% bound for $\tau_X \lesssim 10^6$ sec comes from the constraint that not much more than 90% of the deuterium should be destroyed; for $\tau_X \gtrsim 10^6$ sec the constraint is that deuterium should not be produced from ${}^4\text{He}$ photofission. In Table 3 we show the representative values of $m_X Y_X$ which correspond to 68% and 95% confidence levels respectively, for $\tau_X = 10^4 - 10^9$ sec.

High D ($y_2^{obs} = (1.9 \pm 0.5) \times 10^{-4}$)

In the case of low ${}^4\text{He}$ and high D, SBBN (*i.e.*, low $m_X Y_X$) works quite well for $\eta \sim 2 \times 10^{-10}$. Thus, we expect that we can strongly bound the parameter space of the X -decay model. In Fig. 13, we show the 68% and 95% C.L. contours for some representative values of η . In order to fit to low ${}^4\text{He}$, we can place an upper bound on $m_X Y_X$ at a low η (Fig. 13a).

There are also small allowed (at better than the 68% C.L.) regions of parameter space at higher values of eta (see Figs. 13b – 13d). These allowed regions lie at $\tau_X \gtrsim 10^6$ sec, where a small amount of ${}^4\text{He}$ is broken down into D. However, these allowed regions are small, because the parameters must be finely tuned to target the D abundance to $\sim O(10^{-4})$.

In Fig. 14 we show the contour plots for some representative τ_X in the same manner as Fig. 10.

In Fig. 15 we plot the contours projected along the η axis, in a fashion similar to Fig. 11. Comparing the constraints on τ_X and $m_X Y_X$ with the case of the low D (Fig. 11), we find that the 95% boundary is moved to higher $m_X Y_X$, for $\tau_X \gtrsim 10^6$ sec. This is because D (produced by ${}^4\text{He}$ destruction) is permitted to be an order of magnitude more abundant than in the case of the low D value. We show the 68% and 95% C.L. upper bounds on $m_X Y_X$ in Table 4 at various lifetimes τ_X .

	$\tau_X = 10^4$ sec	10^5 sec	10^6 sec	10^7 sec	10^8 sec	10^9 sec
95% C.L.	5×10^{-6}	5×10^{-9}	6×10^{-10}	5×10^{-10}	7×10^{-11}	4×10^{-11}
68% C.L.	3×10^{-6}	3×10^{-9}	3×10^{-10}	4×10^{-10}	5×10^{-11}	3×10^{-11}

Table 4: Same as Table 3, except for low ${}^4\text{He}$ and high D.

	$\tau_X = 10^4$ sec	10^5 sec	10^6 sec	10^7 sec	10^8 sec	10^9 sec
95% C.L.	7×10^{-6}	7×10^{-9}	8×10^{-10}	1×10^{-10}	8×10^{-12}	3×10^{-12}
68% C.L.	5×10^{-6}	5×10^{-9}	6×10^{-10}	8×10^{-11}	4×10^{-12}	2×10^{-12}

Table 5: Same as Table 3, except for high ${}^4\text{He}$ and low D.

3.3.2 High ${}^4\text{He}$ ($Y^{obs} = 0.244 \pm (0.002)_{stat} \pm (0.005)_{syst}$)

The high observed ${}^4\text{He}$ abundance [Eq. (8)] is consistent with the SBBN theoretical calculations, for both the low and high observed D abundances [Eqs. (5) and (6)]. Therefore, we expect to be able to constrain the model parameters in both cases.

Low D ($y_2^{obs} = (3.39 \pm 0.25) \times 10^{-5}$)

For four representative η values ($\eta_{10} = 2, 4, 5, 6$), we plot the contours of the confidence level in Fig. 16. In Fig. 2, we see that the SBBN calculations agree with the observed abundances for mid-range values of the baryon to photon ratio ($\eta \sim 5 \times 10^{-10}$). Thus, the upper bound for $m_X Y_X$ is plotted in Fig. 16c. Even at a low η (where the SBBN calculation disagrees with the low observed D value), the theoretical calculations can match observed data in the region $10^4 \text{ sec} \lesssim \tau_X \lesssim 10^6 \text{ sec}$ and $m_X Y_X \gtrsim 10^{-10}$, because of the significant destruction of D. In Fig. 17 we show the C.L. plots for three typical lifetimes, $\tau_X = 10^4, 10^5, 10^6$ sec. Finally, we show the C.L. contours projected along the η axis into the $\tau_X - m_X Y_X$ plane (Fig. 18). Table 5 gives the upper bounds on $m_X Y_X$ (GeV) which correspond to 68% and 95% C.L., for some typical values of the lifetime.

High D ($y_2^{obs} = (1.9 \pm 0.5) \times 10^{-4}$)

As in the low D case, we now plot C.L. contours for high D for four typical values of η in Fig. 19. Since the adoption of the high ${}^4\text{He}$ and high D observed values is consistent with SBBN calculations for low η , we expect to obtain bounds on τ_X and $m_X Y_X$ (e.g., Fig. 19a). In Figs. 19b – 19d, we see that we also have allowed regions for $\tau_X \gtrsim 10^6$ sec. The reason is same as the case of low ${}^4\text{He}$ and high D; the D final abundances are well-balanced between production and destruction.

	$\tau_X = 10^4$ sec	10^5 sec	10^6 sec	10^7 sec	10^8 sec	10^9 sec
95% C.L.	2×10^{-6}	3×10^{-9}	3×10^{-10}	4×10^{-10}	5×10^{-11}	3×10^{-11}
68% C.L.	5×10^{-7}	6×10^{-10}	7×10^{-11}	2×10^{-11}	1×10^{-11}	2×10^{-11}

Table 6: Same as Table 3, except for high ${}^4\text{He}$ and high D.

In Fig. 20, we plot the confidence level for $\tau_X = 10^4, 10^5$, and 10^6 sec. The range of preferred η is relatively narrow. This is because the case of high D and high ${}^4\text{He}$ is only consistent in SBBN for low value of η , and in the lifetime range $\tau_X \sim 10^4 - 10^6$, the ${}^4\text{He}$ abundance is not affected by the radiative decay of X .

Next, we show the 68% and 95% C.L. contours projected along the η axis (Fig. 21). There is a large region between the 68% C.L. and the 95% (for a fixed τ_X) for two reasons. First, the uncertainty in the high observed D value is large. Second, the η predicted from the high observed ${}^4\text{He}$ value has a wide spread. The overall shape of the 95% C.L. line is very similar to the case of low ${}^4\text{He}$ and high D. This is because the constraint for $\tau_X \gtrsim 10^6$ sec is particularly sensitive only to the observed D value.

Just as in the case of low ${}^4\text{He}$, the 95% C.L. line for the high D value goes to higher $m_X Y_X$ than for the low D value, because the new D component produced by ${}^4\text{He}$ destruction is allowed to be one order of magnitude larger than in the case of low D. In Table 6, we list the upper bounds on $m_X Y_X$ at the 68% and 95% confidence levels, for various values of τ_X .

3.4 Additional constraints

We now mention additional constraints on our model. First, the the cosmic microwave background radiation (CMBR) was observed by COBE [47] to very closely follow a black-body spectrum. This gives us a severe constraint on particles with lifetime longer than $\sim 10^6$ sec [48], which is when the double Compton process ($\gamma + e^- \rightleftharpoons \gamma + \gamma + e^-$) freezes out [49]. After this time, photon number is conserved, so photon injection from a radiatively decaying particle would cause the spectrum of the CMBR to become a Bose-Einstein distribution with a finite chemical potential μ . COBE [47] observations give us the constraint $|\mu| \lesssim 9.0 \times 10^{-5}$. For small μ , the ratio of the injected to total photon energy density is given by $\delta\rho_\gamma/\rho_\gamma \sim 0.71\mu$. Thus, we have the constraint

$$m_X Y_X \lesssim 1.7 \times 10^{-10} \text{ GeV} \left(\frac{\tau_X}{10^6 \text{ sec}} \right)^{-\frac{1}{2}} \quad \text{for } 10^6 \text{ sec} \lesssim \tau_X \lesssim 4 \times 10^{10} \text{ sec.} \quad (19)$$

Note that for lifetimes τ_X longer than 10^6 sec, the CMBR constraint is stricter than the bounds from the BBN which we have discussed above.

In this paper, we have considered only radiative decays; *i.e.*, decays to photons and invisible particles. If X decays to charged leptons, it is similar in effect to decay to photons

because the charged leptons also generate the electro-magnetic cascade shower. On the other hand if X decays only to neutrinos, the constraints becomes much weaker. In the content of MSSM, the X particle decays to neutrino and sneutrino and the emitted neutrinos scatter off the background neutrinos. Then electron positron pairs are produced and they subsequently produce the many soft photons through the electro-magnetic cascade. Because the interaction between the emitted neutrino and the background neutrino is week, the destruction of the light elements does not occur very efficiently [50]. However, if X decayed to hadrons, we expect that our bounds would tighten, because hadronic showers could be a significant source of D, ${}^3\text{He}$, ${}^6\text{Li}$, ${}^7\text{Li}$, and ${}^7\text{Be}$ [6].

4 Model

So far, we have discussed general constraints from BBN on radiatively decaying particles. In the minimal standard model, there is no such particle. However, some extensions of the standard model naturally result in such exotic particles, and SBBN may be significantly affected in these cases. In this section, we present several examples of such radiatively decaying particles, and discuss the constraints.

Our first example is the gravitino ψ , which appears in all the supergravity models. The gravitino is the superpartner of the graviton, and its interactions are suppressed by inverse powers of the reduced Planck scale $M_* \simeq 2.4 \times 10^{18}$ GeV. Because of this suppression, the lifetime of the gravitino is very long. Assuming that the gravitino's dominant decay mode is to a photon and its superpartner (the photino), the gravitino's lifetime is given by

$$\tau_{3/2} \simeq 4 \times 10^5 \text{ sec} \times (m_{3/2}/1 \text{ TeV})^{-3}, \quad (20)$$

where $m_{3/2}$ is the gravitino mass. Notice that the gravitino mass is $O(100 \text{ GeV} - 1 \text{ TeV})$ in a model with gravity-mediated supersymmetry (SUSY) breaking, resulting in a lifetime which may affect BBN.

If the gravitino is thermally produced in the early universe, and decays without being diluted, it completely spoils the success of SBBN. Usually, we solve this problem by introducing inflation which dilutes away the primordial gravitinos. However, even with inflation, gravitinos are produced through scattering processes of thermal particles after reheating. The abundance $Y_{3/2} = n_{3/2}/n_\gamma$ of the gravitino depends on the reheating temperature T_R , and is given by [4]

$$Y_{3/2} \simeq 2 \times 10^{-11} \times (T_R/10^{10} \text{ GeV}). \quad (21)$$

Therefore, if the reheating temperature is too high, then gravitinos are overproduced, and too many light nuclei are photodissociated.

We can transform our constraints on $(\tau_X, m_X Y_X)$ to constraints on $(m_{3/2}, T_R)$. In particular, we use the projected 95% C.L. boundaries from Figs. 11, 15, 18, and 21. For

several values of the gravitino mass, we read off the most conservative upper bound on the reheating temperature from Fig. 22, and the results are given by

$$\begin{aligned} m_{3/2} = 100 \text{ GeV} \quad (\tau_{3/2} \simeq 4 \times 10^8 \text{ sec}) &: T_R \lesssim 3 \times 10^8 \text{ GeV}, \\ m_{3/2} = 1 \text{ TeV} \quad (\tau_{3/2} \simeq 4 \times 10^5 \text{ sec}) &: T_R \lesssim 1 \times 10^9 \text{ GeV}, \\ m_{3/2} = 3 \text{ TeV} \quad (\tau_{3/2} \simeq 1 \times 10^4 \text{ sec}) &: T_R \lesssim 3 \times 10^{11} \text{ GeV}. \end{aligned}$$

If the gravitino is heavy enough ($m_{3/2} \gtrsim 5 \text{ TeV}$), then its lifetime is too short to destroy even D. In this case, our only constraint is from the overproduction of ${}^4\text{He}$. If the gravitino mass is lighter, then the lifetime is long enough to destroy D or even ${}^4\text{He}$. In this case, our constraint on the reheating temperature is more severe.

Another example of our decaying particle is the lightest superparticle in the MSSM sector, if it is heavier than the gravitino. In particular, if the lightest neutralino is the lightest superparticle in the MSSM sector, then it can be a source of high energy photons, since it will decay into a photon and a gravitino. In this case, we may use BBN to constrain the MSSM.

The abundance of the lightest neutralino is determined when it freezes out of the thermal bath. The abundance is a function of the masses of the superparticles, and it becomes larger as the superparticles gets heavier. Thus, the upper bound on $m_X Y_X$ can be translated into an upper bound on the mass scale of the superparticles.

In order to investigate this scenario, we consider the simplest case where the lightest neutralino is (almost) purely bino \tilde{B} . In this case, the lightest neutralino pair-annihilates through squark and slepton exchange. In particular, if the right-handed sleptons are the lightest sfermions, then the dominant annihilation is $\tilde{B} + \tilde{B} \rightarrow l^+ + l^-$. The annihilation cross section though this process is given by [51]

$$\langle \sigma v_{\text{rel}} \rangle = 8\pi\alpha_1^2 \langle v^2 \rangle \left\{ \frac{m_{\tilde{B}}^2}{(m_{\tilde{B}}^2 + m_{\tilde{l}_R}^2)^2} - \frac{2m_{\tilde{B}}^4}{(m_{\tilde{B}}^2 + m_{\tilde{l}_R}^2)^3} + \frac{2m_{\tilde{B}}^6}{(m_{\tilde{B}}^2 + m_{\tilde{l}_R}^2)^4} \right\}, \quad (22)$$

where $\langle v^2 \rangle$ is the average velocity squared of bino, and we added the contributions from all three generations by assuming the right-handed sleptons are degenerate.³ With this annihilation cross section, the Boltzmann equation for the number density of binos is given by

$$\dot{n}_{\tilde{B}} + 3Hn_{\tilde{B}} = -2\langle \sigma v_{\text{rel}} \rangle (n_{\tilde{B}}^2 - (n_{\tilde{B}}^{\text{EQ}})^2), \quad (23)$$

where $n_{\tilde{B}}^{\text{EQ}}$ is the equilibrium number density of bino. The factor 2 is present because two binos annihilate into leptons in one collision. We solved this equation and obtained the mass density of the bino as a function of the bino mass and the right-handed slepton

³If the bino is heavier than the top quark, then the *s*-wave contribution annihilating into top quarks becomes important. In this paper, we do not consider this case.

mass. (For details, see *e.g.* Ref. [52]). Numerically, for $m_{\tilde{B}} = 100$ GeV, $m_X Y_X$ ranges from $\sim 10^{-9}$ GeV to $\sim 10^{-5}$ GeV as we vary $m_{\tilde{l}_R}$ from 100 GeV to 1 TeV. If $m_X Y_X$ is in this range, BBN is significantly affected unless the lifetime of the bino is shorter than $10^4 - 10^5$ sec (see Tables 3 – 6). The lifetime of the bino is given by

$$\tau_{\tilde{B}} = \left[\frac{1}{48\pi} \frac{m_{\tilde{B}}^5 \cos^2 \theta_W}{m_{3/2}^2 M_*^2} \right]^{-1} \simeq 7 \times 10^4 \text{ sec} \times \left(\frac{m_{\tilde{B}}}{100 \text{ GeV}} \right)^{-5} \left(\frac{m_{3/2}}{1 \text{ GeV}} \right)^2. \quad (24)$$

Notice that the lifetime becomes shorter as the gravitino mass decreases; hence, too much D and ^7Li are destroyed if the gravitino mass is too large. Therefore, we can convert the constraints given in Figs. 11, 15, 18, and 21 into upper bounds on the gravitino mass. Since the abundance of the bino is an increasing function of the slepton mass $m_{\tilde{l}_R}$, the upper bound on the gravitino mass is more severe for larger slepton masses. For example, for $m_{\tilde{B}} = 100$ GeV, the upper bound on the gravitino mass is shown in Fig. 23. At some representative values of the slepton mass the constraint is given by

$$\begin{aligned} m_{\tilde{l}_R} = 100 \text{ GeV} &: m_{3/2} \lesssim 1 \text{ GeV}, \\ m_{\tilde{l}_R} = 300 \text{ GeV} &: m_{3/2} \lesssim 500 \text{ MeV}, \\ m_{\tilde{l}_R} = 1 \text{ TeV} &: m_{3/2} \lesssim 400 \text{ MeV}. \end{aligned}$$

As expected, for a larger value of the slepton mass, the primordial abundance of bino gets larger, and the upper bound on the gravitino mass becomes smaller.

Another interesting source of high energy photons is a modulus field ϕ . Such fields are predicted in string-inspired supergravity theories. A modulus field acquires mass from SUSY breaking, so we estimate its mass m_ϕ to be of the same order as the gravitino mass (see for example [53]).

In the early universe, the mass of the modulus field is negligible compared to the expansion rate of the universe, so the modulus field may sit far from the minimum of its potential. Since the only scale parameter in supergravity is the Planck scale M_* , the initial amplitude ϕ_0 is naively expected to be of $O(M_*)$. However, this initial amplitude is too large; it leads to well-known problems such as matter domination and distortion of the CMBR. Here, we regard ϕ_0 as a free parameter and derive an upper bound on it.

Once the expansion rate becomes smaller than the mass of the modulus field, the modulus field starts oscillating. During this period, the energy density of ϕ is proportional to R^{-3} (where R is the scale factor); hence, its energy density behaves like that of non-relativistic matter. The modulus eventually decays, when the expansion rate becomes comparable to its decay rate. Without entropy production from another source, the modulus density at the decay time is approximately

$$m_\phi Y_\phi = \frac{\rho_\phi}{n_\gamma} \sim 2 \times 10^{10} \text{ GeV} \times (m_\phi/1 \text{ TeV})^{1/2} (\phi_0/M_*)^2, \quad (25)$$

where ρ_ϕ is the energy density of the modulus field. As in our other models, we can convert our constraints on $(\tau_X, m_X Y_X)$ (Figs. 11, 15, 18, and 21) into constraints on

(m_ϕ, ϕ_0) . Using the most conservative of these constraints, we still obtain very stringent bounds on the initial amplitude of the modulus field ϕ_0 :

$$\begin{aligned} m_\phi = 100 \text{ GeV} \quad (\tau_\phi \sim 4 \times 10^8 \text{ sec}) &: \phi_0 \lesssim 2 \times 10^8 \text{ GeV}, \\ m_\phi = 1 \text{ TeV} \quad (\tau_\phi \sim 4 \times 10^5 \text{ sec}) &: \phi_0 \lesssim 7 \times 10^8 \text{ GeV}, \\ m_\phi = 3 \text{ TeV} \quad (\tau_\phi \sim 1 \times 10^4 \text{ sec}) &: \phi_0 \lesssim 2 \times 10^{10} \text{ GeV}. \end{aligned}$$

Clearly, our upper bound from BBN rules out our naive expectation that $\phi_0 \sim M_*$. It is important to notice that (conventional) inflation cannot solve this difficulty by diluting the coherent mode of the modulus field. This is because the expansion rate of the universe is usually much larger than the mass of the modulus field, and hence the modulus field does not start oscillation. One attractive solution is a thermal inflation model proposed by Lyth and Stewart [54]. In the thermal inflation model, a mini-inflation with e -fold number ~ 10 reduces the modulus density. Even if thermal inflation occurs, there may remain a significant modulus energy density, which decays to high energy photons. Thus, BBN gives a stringent constraint on the thermal inflation model.

5 Discussion and Conclusions

We have discussed the photodissociation of light elements due to the radiative decay of a massive particle, and we have shown how we can constrain our model parameters from the observed light-element abundances. We adopted two D values and two ${}^4\text{He}$ values in this paper, and we obtained constraints on the properties of the radiatively decaying particle in each case.

When we adopt the low ${}^4\text{He}$ and low D values, we find that a non-vanishing amount of such a long-lived, massive particle is preferred: $m_X Y_X \gtrsim 10^{-10} \text{ GeV}$ for $10^4 \text{ sec} \lesssim \tau_X \lesssim 10^6 \text{ sec}$. On the other hand, consistency with the observations imposes upper bounds on $m_X Y_X$ in each of the four cases.

We have also studied the photodissociation of ${}^7\text{Li}$ and ${}^6\text{Li}$ in this paper. These processes do not affect the D and ${}^4\text{He}$ abundances, because ${}^7\text{Li}$ and ${}^6\text{Li}$ are many orders of magnitude less abundant than D and ${}^4\text{He}$. When we examine the region of parameter space where the predicted abundances agree well with the observed ${}^7\text{Li}$ and the low ${}^4\text{He}$ and low D observations, we find that the produced ${}^6\text{Li}/\text{H}$ may be of order 10^{-12} , which is two orders of magnitude larger than the prediction of SBBN (see Figs. 7 and 12). The predicted ${}^6\text{Li}$ is consistent with the observed upper bound Eq. (10) throughout the region of parameter space we are interested in. Although presently it is believed that the observed ${}^6\text{Li}$ abundance is produced by spallation, our model suggests another origin: the observed ${}^6\text{Li}$ may be produced by the photodissociation of ${}^7\text{Li}$.

We have also discussed candidates for our radiatively decaying particle. Our first example is the gravitino. In this case, we can constrain the reheating temperature after inflation, because it determines the abundance of the gravitino. We obtained the stringent

bounds $T_R \lesssim 10^8 \text{GeV} - 10^9 \text{GeV}$ for $100 \text{ GeV} \lesssim m_{3/2} \lesssim 1 \text{ TeV}$. Our second example is the lightest neutralino which is heavier than the gravitino. When the neutralino is the lightest superparticle in the MSSM sector, it can decay into a photon and a gravitino. If we assume the lightest neutralino is pure bino, and its mass is about 100 GeV, the relic number density of binos is related to the right-handed slepton mass, because they annihilate mainly through right-handed slepton exchange. For this case, we obtained the upper bound of the gravitino mass, $m_{3/2} \lesssim 400 \text{ MeV} - 1 \text{ GeV}$ for $100 \text{ GeV} \lesssim m_{\tilde{l}_R} \lesssim 1 \text{ TeV}$. Our third example is a modulus field. We obtained a severe constraint on its initial amplitude, $\phi_0 \lesssim 10^8 \text{ GeV} - 10^{10} \text{ GeV}$ for $100 \text{ GeV} \lesssim m_{3/2} \lesssim 1 \text{ TeV}$. This bound is well below the Planck scale, so it suggests the need for a dilution mechanism, such as thermal inflation.

Acknowledgement

This work was supported by the Director, Office of Energy Research, Office of Basic Energy Services, of the U.S. Department of Energy under Contract DE-AC03-76SF00098. K.K. is supported by JSPS Research Fellowship for Young Scientists.

A Appendix

In this appendix, we explain how we answer the question, “How well does our simulation of BBN agree with the observed light-element abundances?” To be more precise, we rephrase the question as, “At what confidence level is our simulation of BBN excluded by the observed light-element abundances?”

From our Monte-Carlo BBN simulation, we obtain the theoretical probability density function (p.d.f.) $p^{th}(\mathbf{a}^{th})$ of our simulated light-element abundances $\mathbf{a}^{th} = (y_2^{th}, Y^{th}, \log_{10} y_7^{th})$. We find that $p^{th}(\mathbf{a}^{th})$ is well-approximated by a multivariate Gaussian. (See Eqs. (11) and (12).) Note that $p^{th}(\mathbf{a}^{th})$ depends upon the parameters \mathbf{p} of our theory, *e.g.* $\mathbf{p} = (\eta, \dots)$. (The ellipses refer to parameters in non-standard BBN, *e.g.*, m_X , Y_X , τ_X .) In particular, the means and standard deviations of $p^{th}(\mathbf{a}^{th})$ are functions of \mathbf{p} .

We also construct the p.d.f. $p^{obs}(\mathbf{a}^{obs})$ for the observed light-element abundances, *viz.* $\mathbf{a}^{obs} = (y_2^{obs}, Y^{obs}, \log_{10} y_7^{obs})$. Since the observations of the light element abundances are independent, we can factor

$$p^{obs}(\mathbf{a}^{obs}) = p_2^{obs}(y_2^{obs}) \times p_4^{obs}(Y^{obs}) \times p_7^{obs}(\log_{10} y_7^{obs}) \quad (26)$$

We assume Gaussian p.d.f.’s for y_2^{obs} , Y^{obs} , and $\log_{10} y_7^{obs}$. We use the mean abundances and standard deviations given in Equations (5)–(9). Since we have two discordant values of D/H and two discordant values of ${}^4\text{He}$, we considered four cases (each with its own p.d.f. $p^{obs}(\mathbf{a}^{obs})$): (i) low ${}^4\text{He}$, low D/H; (ii) low ${}^4\text{He}$, high D/H; (iii) high ${}^4\text{He}$, low D/H; and (iv) high ${}^4\text{He}$, high D/H.

Then $\Delta\mathbf{a} = \mathbf{a}^{th} - \mathbf{a}^{obs}$ has a p.d.f. given by

$$\begin{aligned} p^\Delta(\Delta\mathbf{a}) &= \int d\mathbf{a}^{obs} p^{obs}(\mathbf{a}^{obs}) \int d\mathbf{a}^{th} p^{th}(\mathbf{a}^{th}) \delta(\Delta\mathbf{a} - (\mathbf{a}^{th} - \mathbf{a}^{obs})) \\ &= \int d\mathbf{a} p^{th}(\mathbf{a}) p^{obs}(\mathbf{a} - \Delta\mathbf{a}), \end{aligned} \quad (27)$$

where we have suppressed the dependence of $p^\Delta(\Delta\mathbf{a})$ and $p^{th}(\mathbf{a}^{th})$ on the theory parameters \mathbf{p} . Note that when all p_i^{th} and p_i^{obs} are Gaussian, Eq. (27) is easily integrated to yield a product of three Gaussian p.d.f.'s.

$$p^\Delta(\Delta\mathbf{a}) = \prod_i \frac{1}{\sqrt{2\pi}\sigma_i} \exp\left[-\frac{(\Delta a_i - \Delta \bar{a}_i)^2}{2\sigma_i^2}\right], \quad (28)$$

where $\Delta \bar{a}_i = \bar{a}_i^{th} - \bar{a}_i^{obs}$, $\sigma_i^2 = (\sigma_i^{th})^2 + (\sigma_i^{obs})^2$, and i runs over y_2 , Y and $\log_{10}y_7$.

Our question can now be rephrased as, “At what confidence level is $\Delta\mathbf{a} = 0$ excluded?” The answer,

$$\text{C.L.}(\mathbf{p}) = \int_{\{\Delta\mathbf{a}: p^\Delta(\Delta\mathbf{a}; \mathbf{p}) > p^\Delta(0; \mathbf{p})\}} d(\Delta\mathbf{a}) p^\Delta(\Delta\mathbf{a}; \mathbf{p}), \quad (29)$$

is used in this paper to constrain various scenarios of BBN. Since we have assumed Gaussian p.d.f.'s, we can easily evaluate this integral. The result is conveniently expressed in terms of χ^2 . (See Eqs. (13) and (15).)

Our confidence level is calculated for three degrees of freedom Δa_i . It denotes our certainty that a given point \mathbf{p} in the parameter space of the theory is excluded by the observed abundances. If the abundances a_i were linear in the theory parameters \mathbf{p} , then we could integrate out a theory parameter such as η and set a C.L. exclusion limit (with a reduced number of degrees of freedom) on the remaining parameters. However, the a_i turn out to be highly non-linear, so such a procedure turns out to have little meaning. Instead, we shall project out various theory parameters (as explained in Section 3.3.1) to present our results as graphs.

References

- [1] T.P. Walker, G. Steigman, D.N. Schramm, K.A. Olive, and H.-S. Kang, *Astrophys. J.* **376** (1991) 51.
- [2] D. Lindley, *Mon. Not. Roy. Astron. Soc.* **188** (1979) 15P; D. Lindley, *Astrophys. J.* **294** (1985) 1.
- [3] H. Pagels and J.R. Primack, *Phys. Rev. Lett.* **48** (1982) 223; S. Weinberg, *Phys. Rev. Lett.* **48** (1982) 1303; L.M. Krauss, *Nucl. Phys.* **B227** (1983) 556; J. Ellis, E. Kim, and D.V. Nanopoulos, *Phys. Lett.* **B145** (1984) 181; R. Juszkiewicz, J. Silk, and A.

Stebbins, *Phys. Lett.* **B158** (1985) 463; M. Kawasaki and K. Sato, *Phys. Lett.* **B189** (1987) 23; J. Ellis, G.B. Gelmini, J.L. Lopez, D.V. Nanopoulos, and S. Sarkar, *Nucl. Phys.* **B373** (1992) 399; T. Moroi, H. Murayama, and M. Yamaguchi, *Phys. Lett.* **B303** (1993) 289.

[4] M. Kawasaki and T. Moroi, *Prog. Theor. Phys.* **93** (1995) 879, hep-ph/9403364.

[5] M. Kawasaki and T. Moroi, *Astrophys. J.* **452** (1995) 506, astro-ph/9412055.

[6] S. Dimopoulos, R. Esmailzadeh, L.J. Hall, and G.D. Starkman, *Astrophys. J.* **330** (1988) 545; *Nucl. Phys.* **B311** (1989) 699.

[7] N. Hata, R.J. Scherrer, G. Steigman, D. Thomas, T.P. Walker, S. Bludman, and P. Langacker, *Phys. Rev. Lett.* **75** (1995) 3977, hep-ph/9505319.

[8] K. Kohri, M. Kawasaki, and K. Sato, *Astrophys. J.* **490** (1997) 72, astro-ph/9612237.

[9] M. Kawasaki, K. Kohri, and K. Sato, *Phys. Lett.* **B** in press, astro-ph/9705148.

[10] E. Holtmann, M. Kawasaki, and T. Moroi, *Phys. Rev. Lett.* **77** (1996) 3712, hep-ph/9603241.

[11] A. Songaila, L.L. Cowie, C.J. Hogan, and M. Rugers, *Nature* **368** (1994) 599.

[12] M. Rugers and C.J. Hogan, *Astron. J.* **111** (1996) 2135, astro-ph/9603084; J. K. Webb *et al.*, *Nature* **388** (1997) 250.

[13] M. Rugers and C.J. Hogan, *Astrophys. J., Lett.* **459** (1996) L1.

[14] S. Burles and D. Tytler, submitted to *Astrophys. J.*, astro-ph/9712109.

[15] B.E.J. Pagel *et al.*, *Mon. Not. R. Astron. Soc.* **255** (1992) 325.

[16] K.A. Olive, G. Steigman, and E.D. Skillman, *Astrophys. J.* **483** (1997) 788.

[17] T.X. Thuan and Y.I. Izotov, in *Primordial Nuclei and their Galactic Evolution*, edited by N. Prantzos, M. Tosi, and R. von Steiger (Kluwer Academic Publications, Dordrecht, 1998) in press.

[18] Y.I. Izotov, T.X. Thuan, and V.A. Lipovetsky, *Astrophys. J. Suppl. Series*, **108** (1997) 1.

[19] C.J. Copi, K.A. Olive, and D.N. Schramm, astro-ph/9606156.

[20] R.F. Carswell, M. Rauch, R.J. Weymann, A.J. Cooke, and J.K. Webb, *Mon. Not. Roy. Astron. Soc.* **268** (1994) L1.

- [21] R.F. Carswell, J.K. Webb, K.M. Lanzetta, *et al.* *Mon. Not. Roy. Astron. Soc.* **278** (1996) 506; M. Rugers and C. Hogan, *Astr. Soc. of the Pacific Conf. Series* **99** (1996) 100; E.J. Wampler, G.M. Williger, J.A. Baldwin, R.F. Carswell, C. Hazard, and R.G. McMahon *Astronomy and Astrophysics* **316** (1996) 33.
- [22] G. Steigman, in *Light Element Abundances. Proceedings of an ESO/EIPC Workshop*, edited by P. Crane, (Springer, Berlin, Germany, 1995), astro-ph/9410060.
- [23] D. Tytler, S. Burles, and D. Kirkman, submitted to *Astrophys. J.*, astro-ph/9612121.
- [24] D. Tytler, X.-M. Fan, and S. Burles, *Nature* **381** (1996) 207, astro-ph/9603069; S. Burles and D. Tytler, submitted to *Science*, astro-ph/9603070.
- [25] E.J. Wampler, *Nature* **383** (1996) 308.
- [26] A. Songaila, E.J. Wampler, and L.L. Cowie, *Nature* **385** (1997) 137, astro-ph/9611143.
- [27] F. Spite and M. Spite, *Astronomy and Astrophysics* **115** (1982), 357.
- [28] P. Bonifacio and P. Molaro, *Mon. Not. Roy. Astron. Soc.* **285** (1997) 847.
- [29] C.J. Hogan, astro-ph/9609138.
- [30] B.D. Fields, K. Kainulainen, K.A. Olive, and D. Thomas, *New Astron.* **1** (1996) 77, astro-ph/9603009.
- [31] L.M. Hobbs and J.A. Thorburn, *Astrophys. J.* **491** (1997) 772.
- [32] V.V. Smith, D.L. Lambert, and P.E. Nissen, *Astrophys. J.* **408** (1993) 262.
- [33] L. Kawano, preprint FERMILAB-Pub-92/04-A.
- [34] Particle Data Group, *Phys. Rev.* **D54** (1996) 1.
- [35] G.R. Caughlan and W.A. Fowler, *Atomic Data and Nuclear Data Tables* **40** (1988) 283; M.S. Smith, L.H. Kawano, and R.A. Malaney, *Astrophys. J. Suppl. Series* **85** (1993) 219.
- [36] J. Yang, M.S. Turner, G. Steigman, D.N. Schramm, and K.A. Olive, *Astrophys. J.* **281** (1984) 493.
- [37] C.J. Copi, D.N. Schramm, and M.S. Turner, *Phys. Rev. Lett.* **75** (1995) 3981, astro-ph/9508029.
- [38] A.A. Zdziarski, *Astrophys. J.* **335** (1988) 786; R. Svensson and A.A. Zdziarski, *Astrophys. J.* **349** (1990) 415.

- [39] R.D. Evans, *The Atomic Nucleus* (McGraw-Hill, New York, 1955).
- [40] R. Pfeiffer, *Z. Phys.* **208** (1968) 129.
- [41] D.D. Faul, B.L. Berman, P. Mayer, and D.L. Olson, *Phys. Rev. Lett.* **44** (1980) 129.
- [42] A.N. Gorbunov and A.T. Varfolomeev, *Phys. Lett.* **11** (1964) 137.
- [43] J.D. Irish, R.G. Johnson, B.L. Berman, B.J. Thomas, K.G. McNeill, and J.W. Jury, *Can. J. Phys.* **53** (1975) 802.
- [44] C.K. Malcom, D.V. Webb, Y.M. Shin, and D.M. Skopik, *Phys. Lett.* **B47** (1973) 433.
- [45] Yu.M. Arkatov, P.I. Vatset, V.I. Voloshchuk, V.A. Zolenko, I.M. Prokhorets, and V.I. Chimir', *Sov. J. Nucl. Phys.* **19** (1974) 598.
- [46] B.L. Berman, *Atomic Data and Nuclear Data Tables* **15** (1975) 319.
- [47] D.J. Fixsen *et al.*, *Astrophys. J.* **473** (1996) 576.
- [48] W. Hu and J. Silk, *Phys. Rev. Lett.* **70** (1993) 2661.
- [49] A.P. Lightman, *Astrophys. J.* **244** (1981) 392.
- [50] J. Gratsias, R.J. Scherrer, and D.N. Spergel, *Phys. Lett.* **B262** (1991) 298; M. Kawasaki and T. Moroi, *Phys. Lett.* **B346** (1995) 27, hep-ph/9408321.
- [51] K.A. Olive and M. Srednicki, *Phys. Lett.* **B230** (1989) 78.
- [52] E.W. Kolb and M.S. Turner, *The Early Universe* (Addison-Wesley, 1990).
- [53] B. de Carlos, J.A. Casas, F. Quevedo, and E. Roulet, *Phys. Lett.* **B318** (1993) 447, hep-ph/9308325.
- [54] D.H. Lyth and E.D. Stewart, *Phys. Rev. Lett.* **75** (1995) 201, hep-ph/9502417; *Phys. Rev.* **D53** (1996) 1784, hep-ph/9510204.

Figure captions

Figure 1: SBBN prediction of the abundances of the light elements. The solid lines are the central values of the predictions, and the dotted lines represents the $1-\sigma$ uncertainties. The boxes denote the $1-\sigma$ observational constraints.

Figure 2: χ^2 as a function of η , for SBBN with three degrees of freedom. We used four combinations of the D and ^4He abundances deduced from observation: low ^4He and low D (short-dashed), low ^4He and high D (dotted-dashed), high ^4He and low D (solid), high ^4He and high D (long-dashed).

Figure 3: C.L. for BBN as a function of η and N_ν , with (a) low value of Y , and (b) high value of Y . The filled square denotes the best fit point.

Figure 4: Photon spectrum $f_\gamma = dn_\gamma/dE_\gamma$ for several background temperatures T_γ^{BG} .

Figure 5: Abundance of D in the $m_X Y_X$ vs. τ_X plane with (a) $\eta = 2 \times 10^{-10}$, (b) $\eta = 4 \times 10^{-10}$, (c) $\eta = 5 \times 10^{-10}$, and (d) $\eta = 6 \times 10^{-10}$.

Figure 6: Same as Fig. 5, except for ^4He .

Figure 7: Same as Fig. 5, except for ^6Li .

Figure 8: Same as Fig. 5, except for ^7Li .

Figure 9: C.L. in the $m_X Y_X$ vs. τ_X plane, for low value of D abundance and low value of Y . We take (a) $\eta = 2 \times 10^{-10}$, (b) $\eta = 4 \times 10^{-10}$, (c) $\eta = 5 \times 10^{-10}$, and (d) $\eta = 6 \times 10^{-10}$. The shaded regions are $y_6/y_7 \gtrsim 0.5$ and the darker shaded regions are $y_6/y_7 \gtrsim 1.3$.

Figure 10: C.L. in the η vs. $m_X Y_X$ plane for various values of τ_X , for low value of D abundance and low value of Y .

Figure 11: Contours of C.L. projected on η axis for low value of D abundance and low value of Y .

Figure 12: Predicted light element abundances ^4He , D, ^7Li and ^6Li at $\tau_X = 10^6$ sec and $m_X Y_X = 5 \times 10^{10}$ GeV. The contours which are favored by observation are plotted, adopting the low ^4He and low D values. The dotted line denotes the 95% C.L. and the shaded region denotes the 68% C.L.. The predicted ^6Li abundance is two orders of magnitude larger than the case of SBBN.

Figure 13: Same as Fig. 9, except for high value of D abundance and low value of Y .

Figure 14: Same as Fig. 10, except for high value of D abundance and low value of Y .

Figure 15: Same as Fig. 12, except for high value of D abundance and low value of Y .

Figure 16: Same as Fig. 9, except for low value of D abundance and high value of Y .

Figure 17: Same as Fig. 10, except for low value of D abundance and high value of Y .

Figure 18: Same as Fig. 12, except for low value of D abundance and high value of Y .

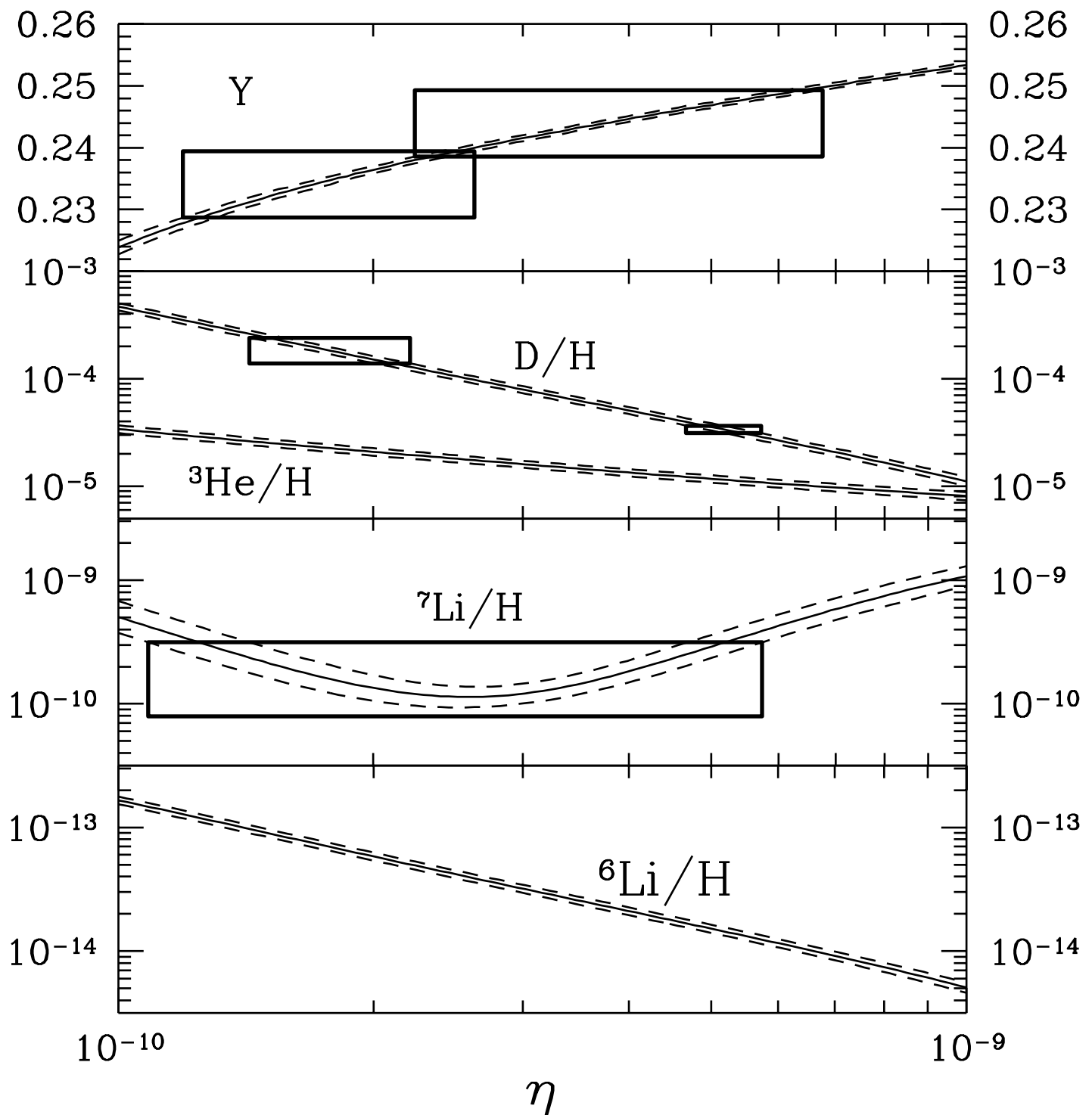
Figure 19: Same as Fig. 9, except for high value of D abundance and high value of Y .

Figure 20: Same as Fig. 10, except for high value of D abundance and high value of Y .

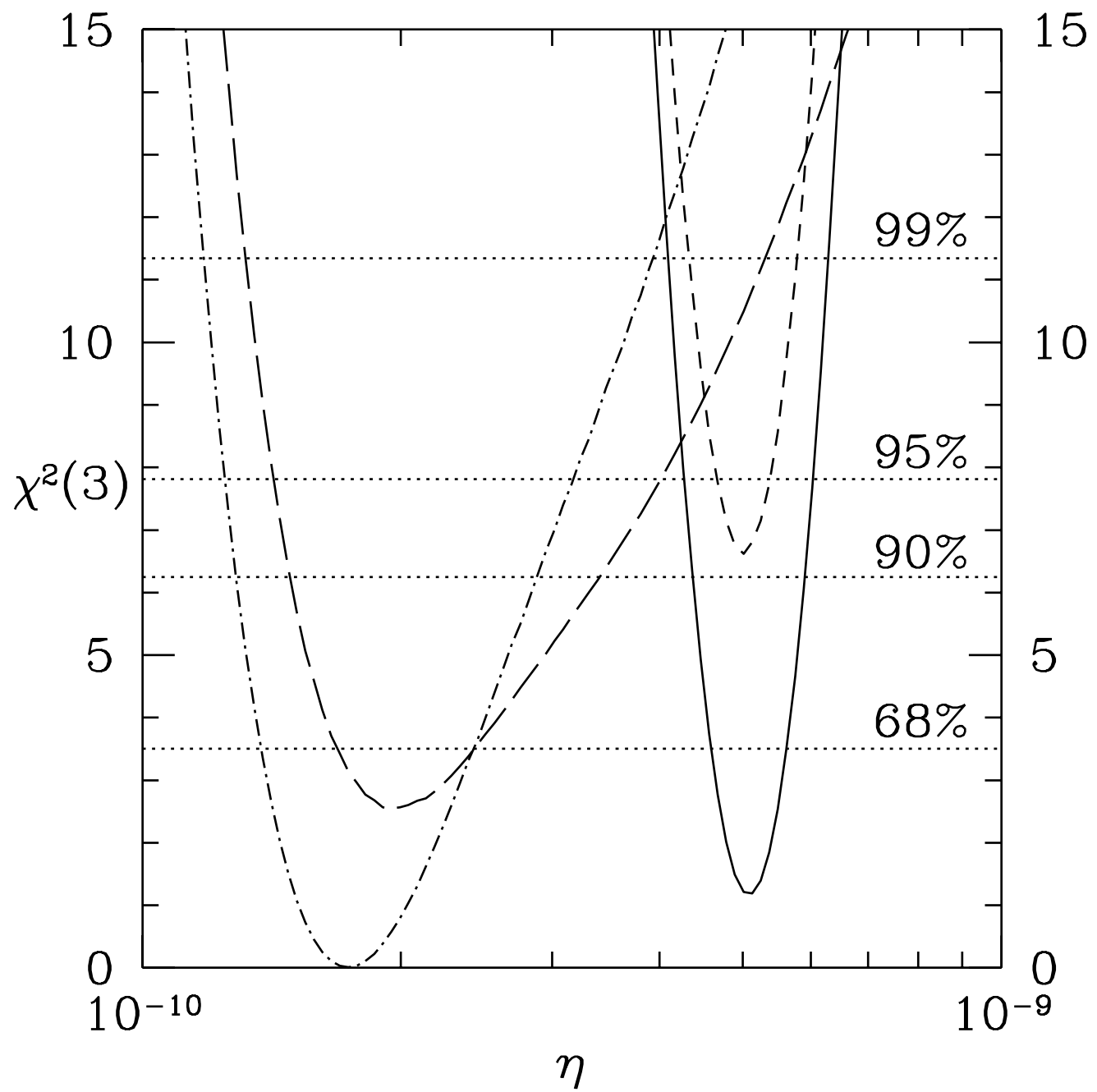
Figure 21: Same as Fig. 12, except for high value of D abundance and high value of Y .

Figure 22: Contours of 95% C.L., yielding an upper bound on the reheating temperature, as a function of the gravitino mass.

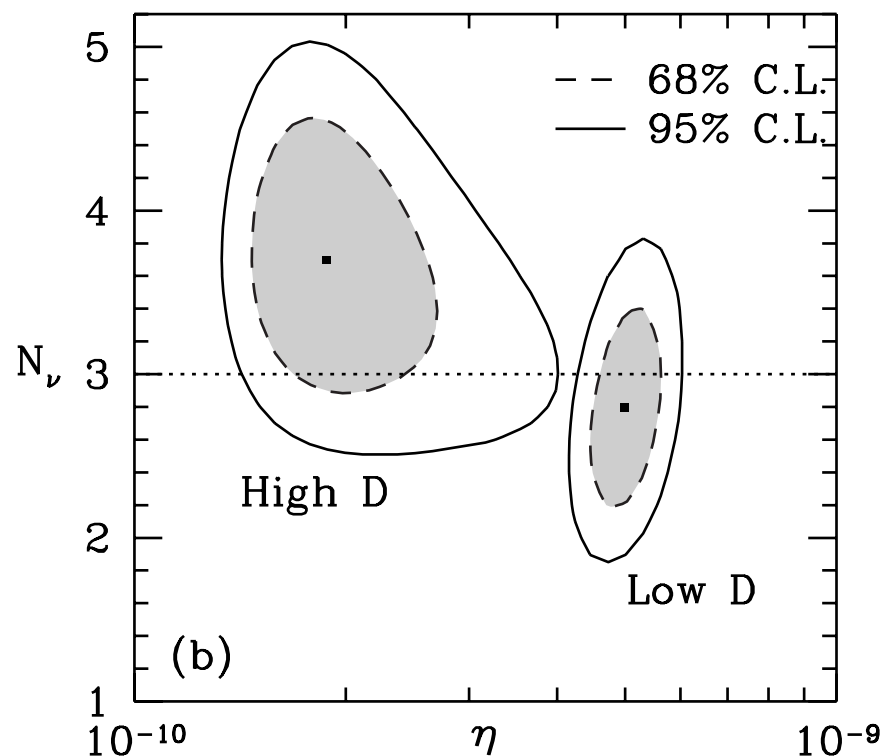
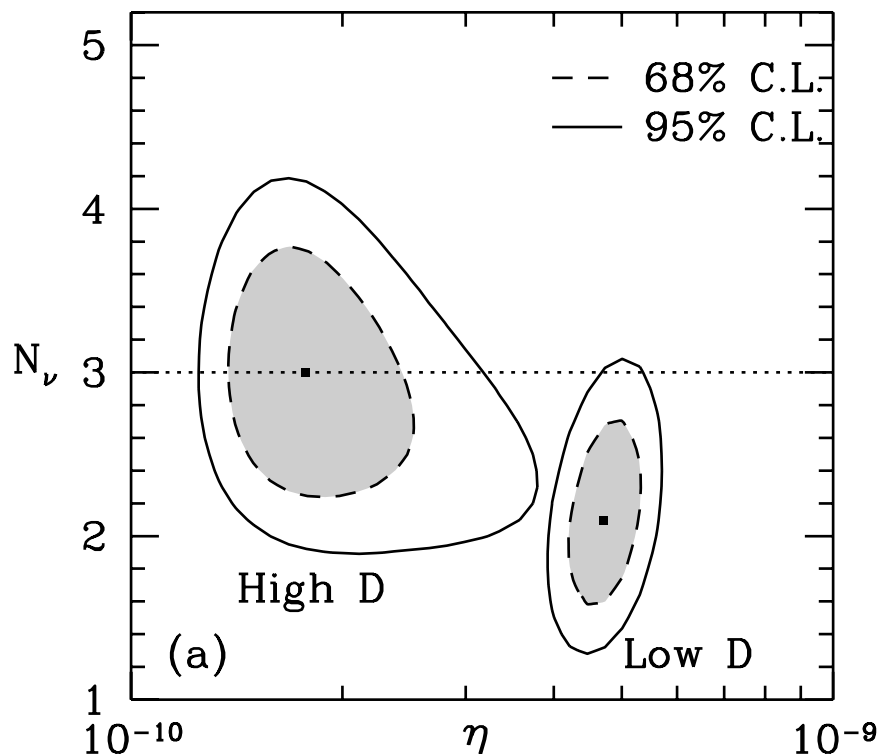
Figure 23: Contours of 95% C.L., yielding an upper bound on the gravitino mass, as a function of the right-handed slepton mass.



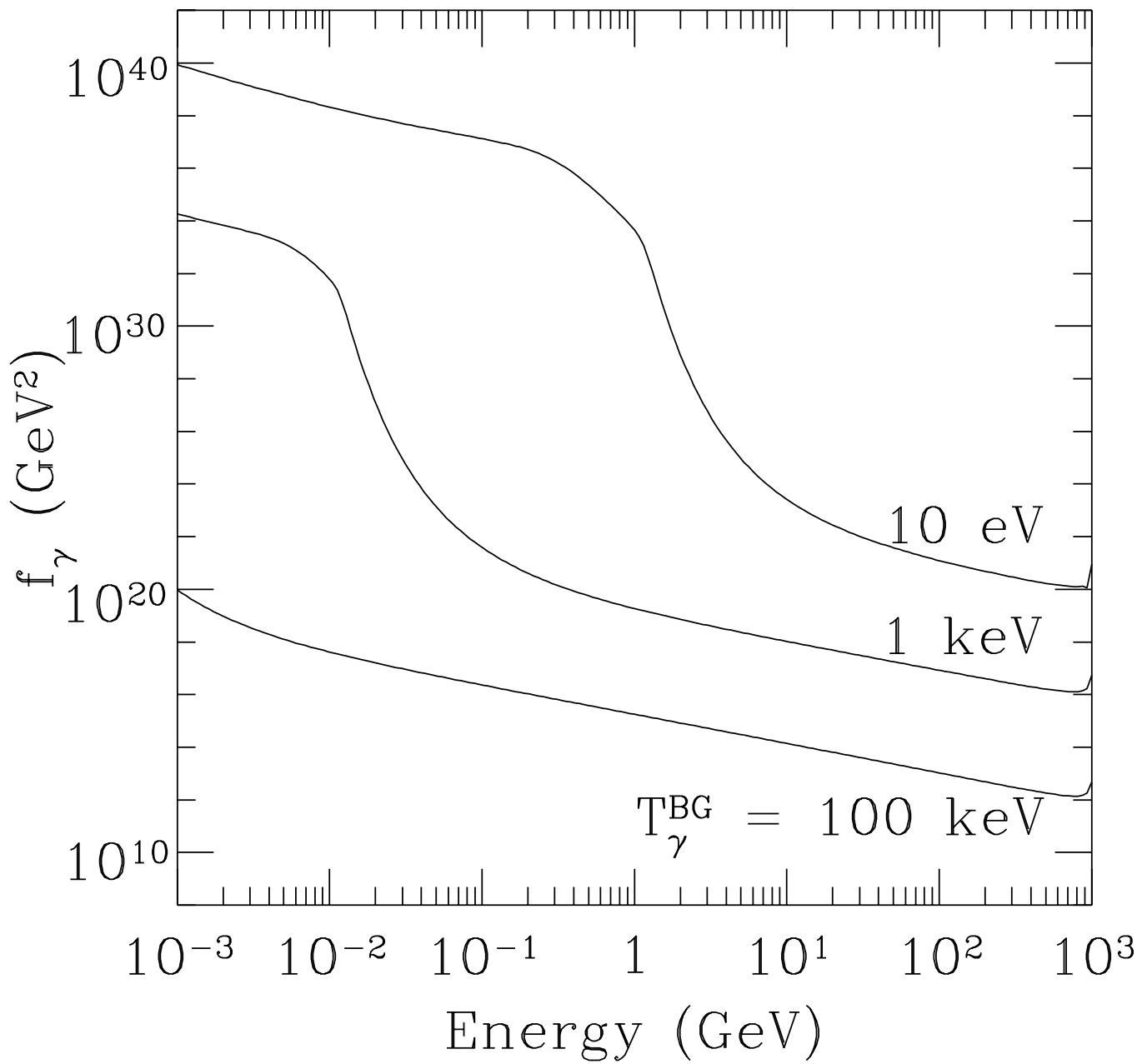
E. Holtmann et al. Fig. 1



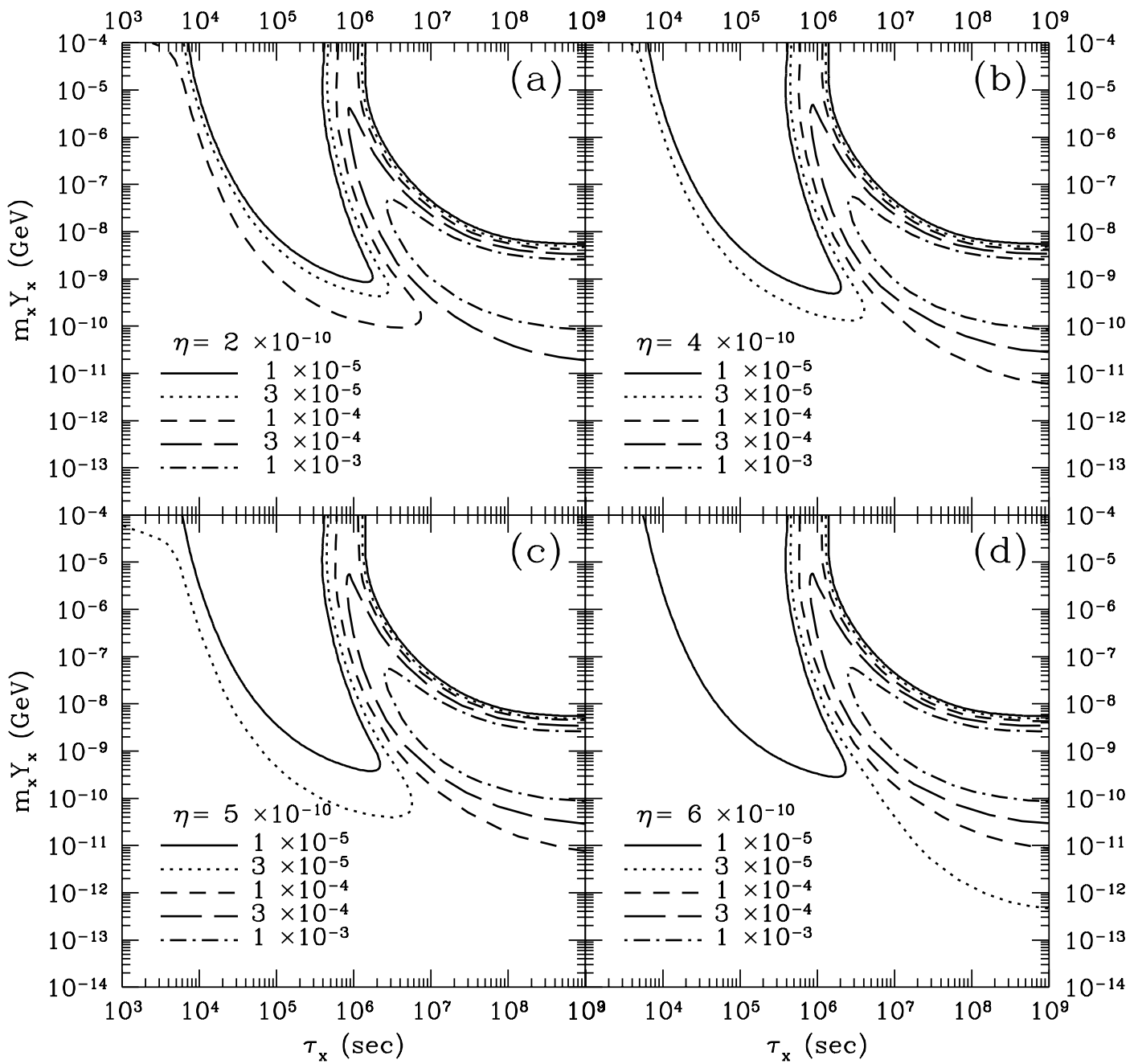
E. Holtmann et al. Fig. 2



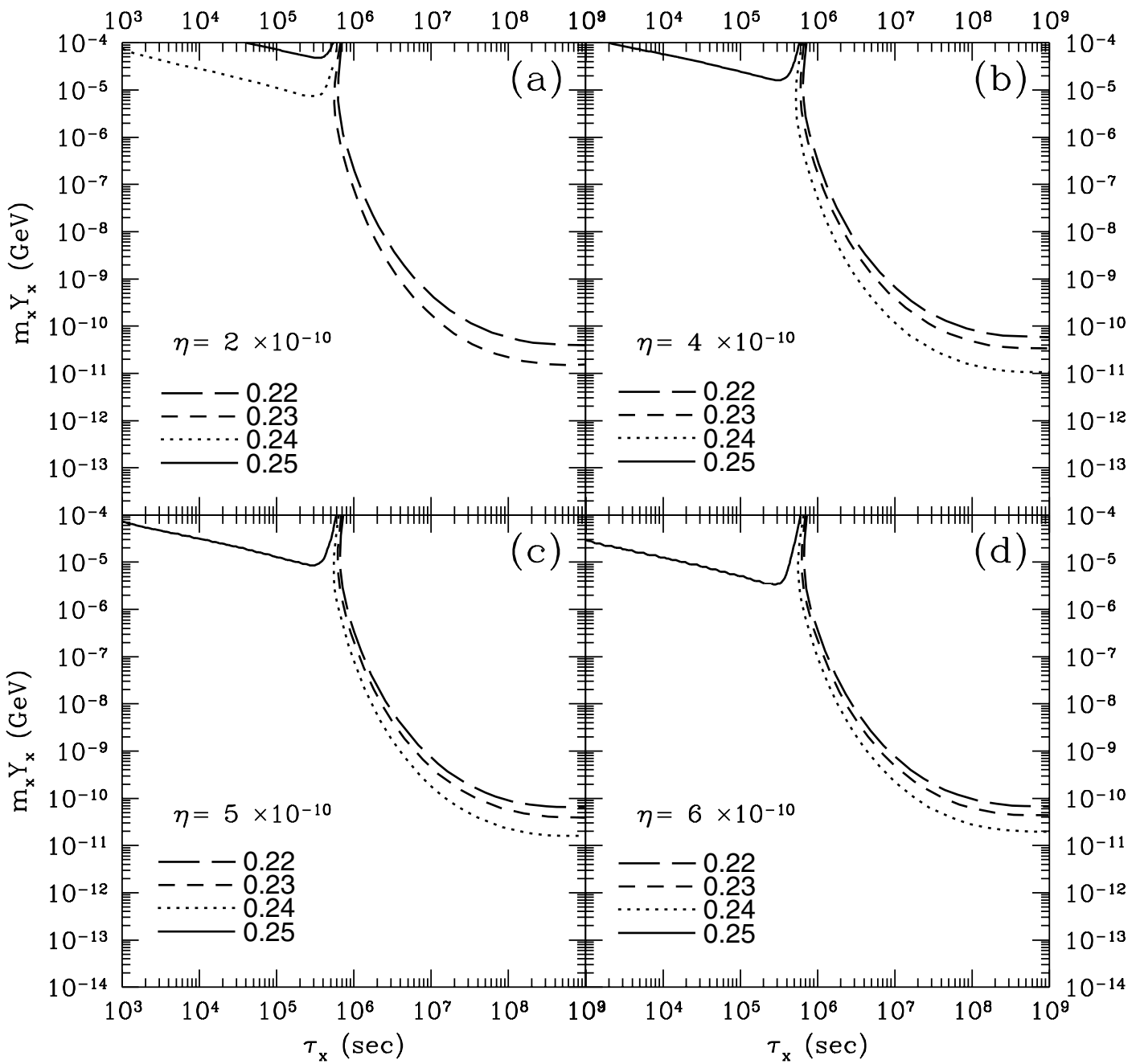
E. Holtmann et al. Fig. 3



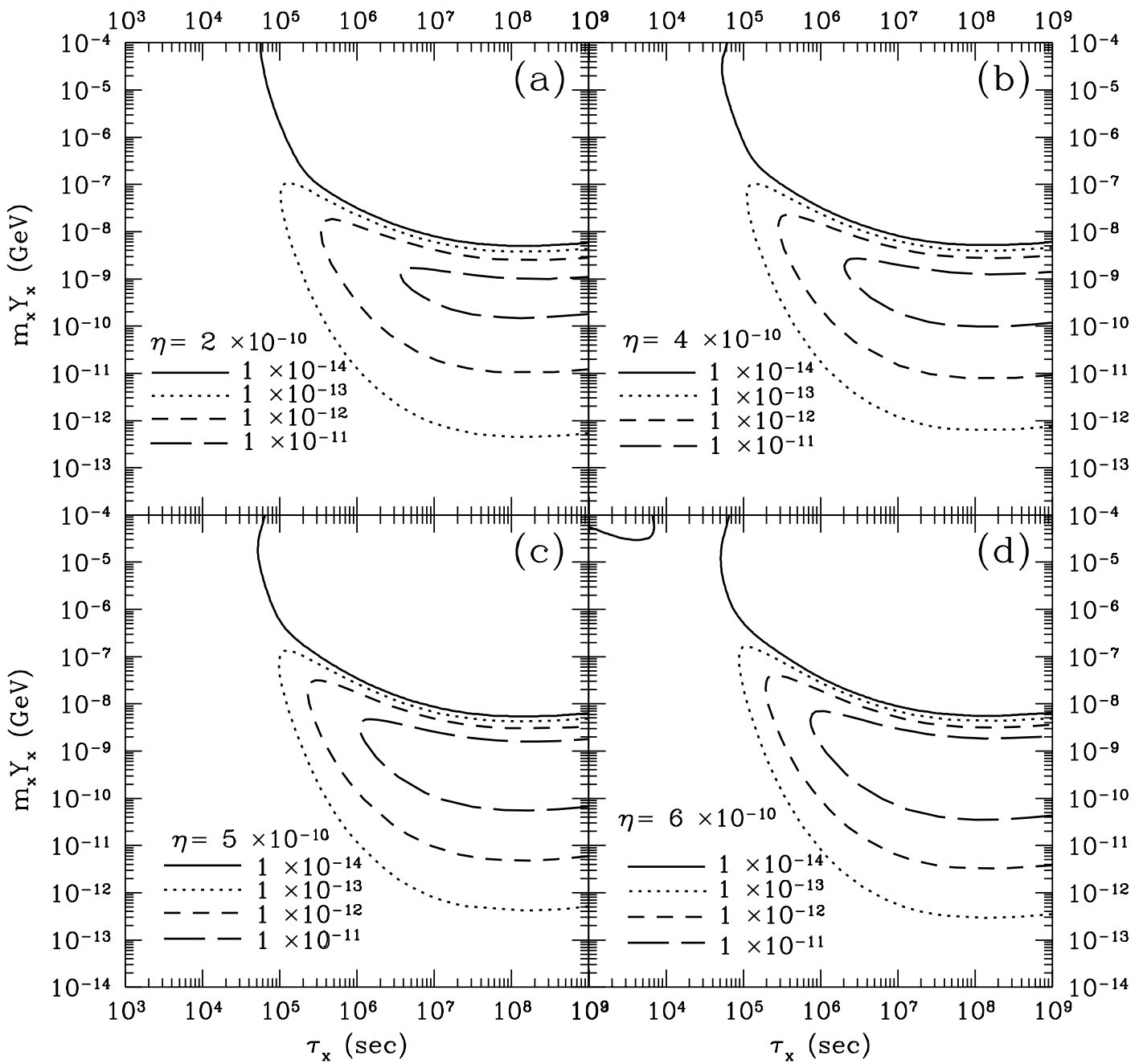
E. Holtmann et al. Fig. 4



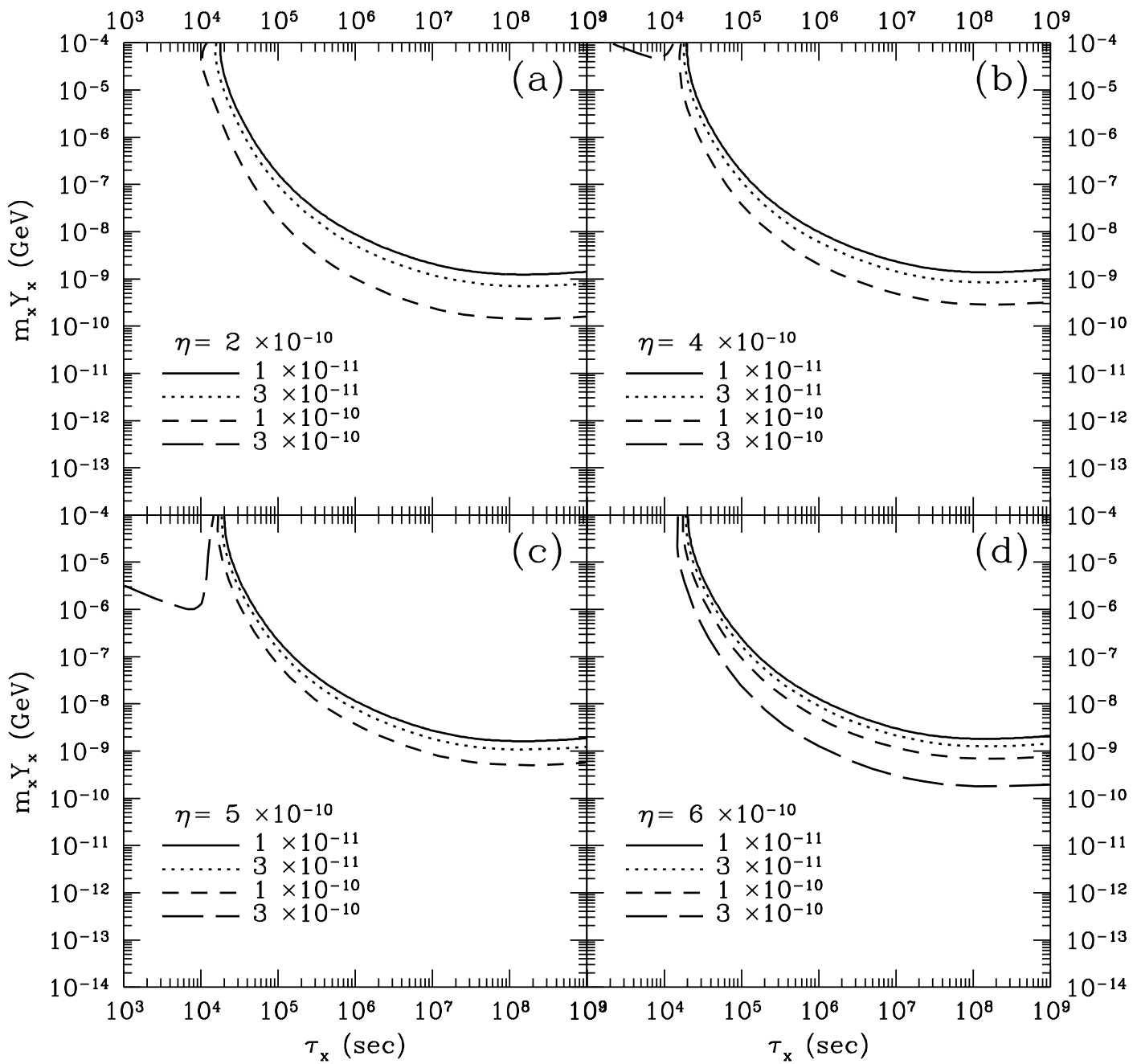
E. Holtmann et al. Fig. 5



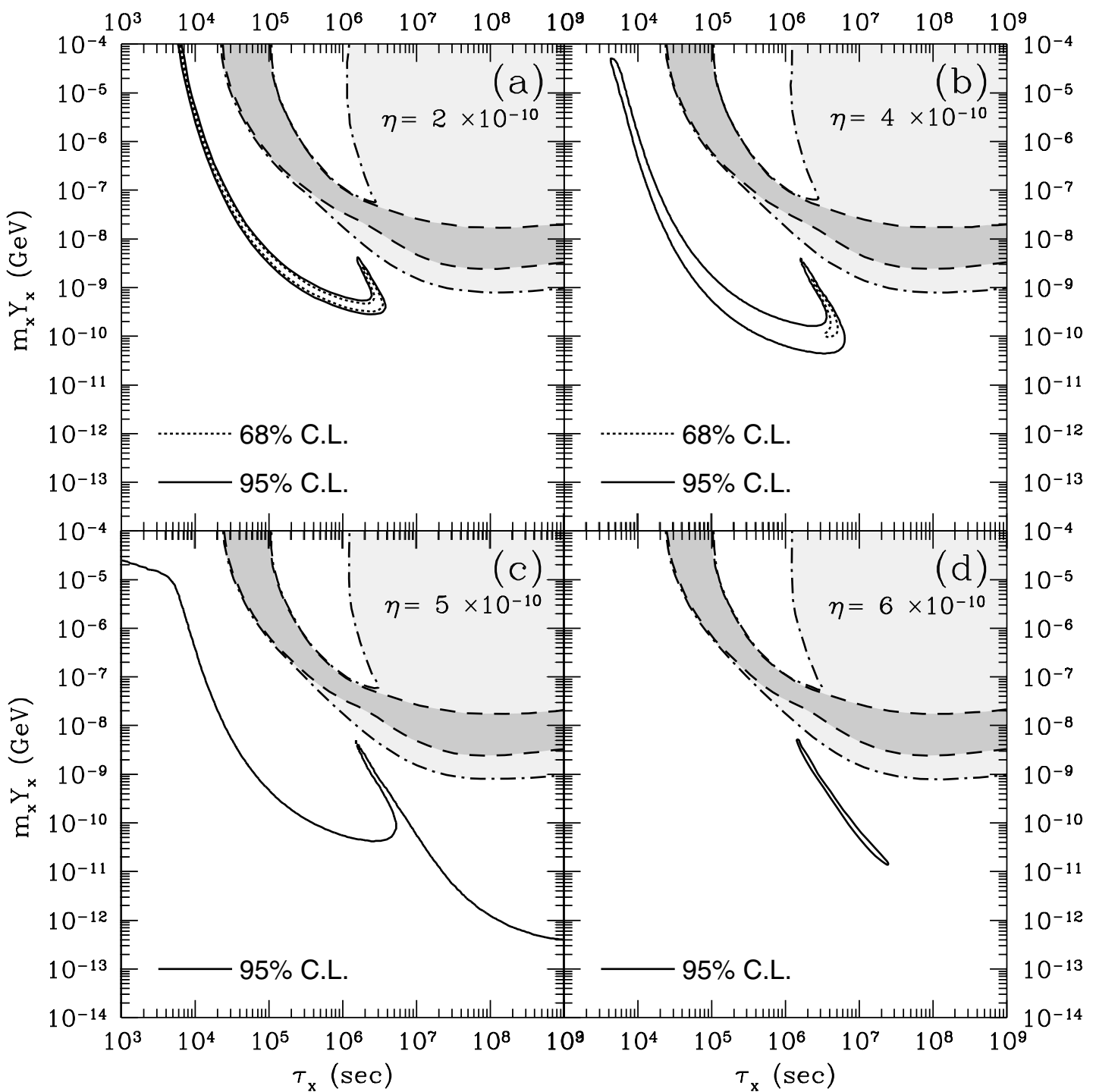
E. Holtmann et al. Fig. 6



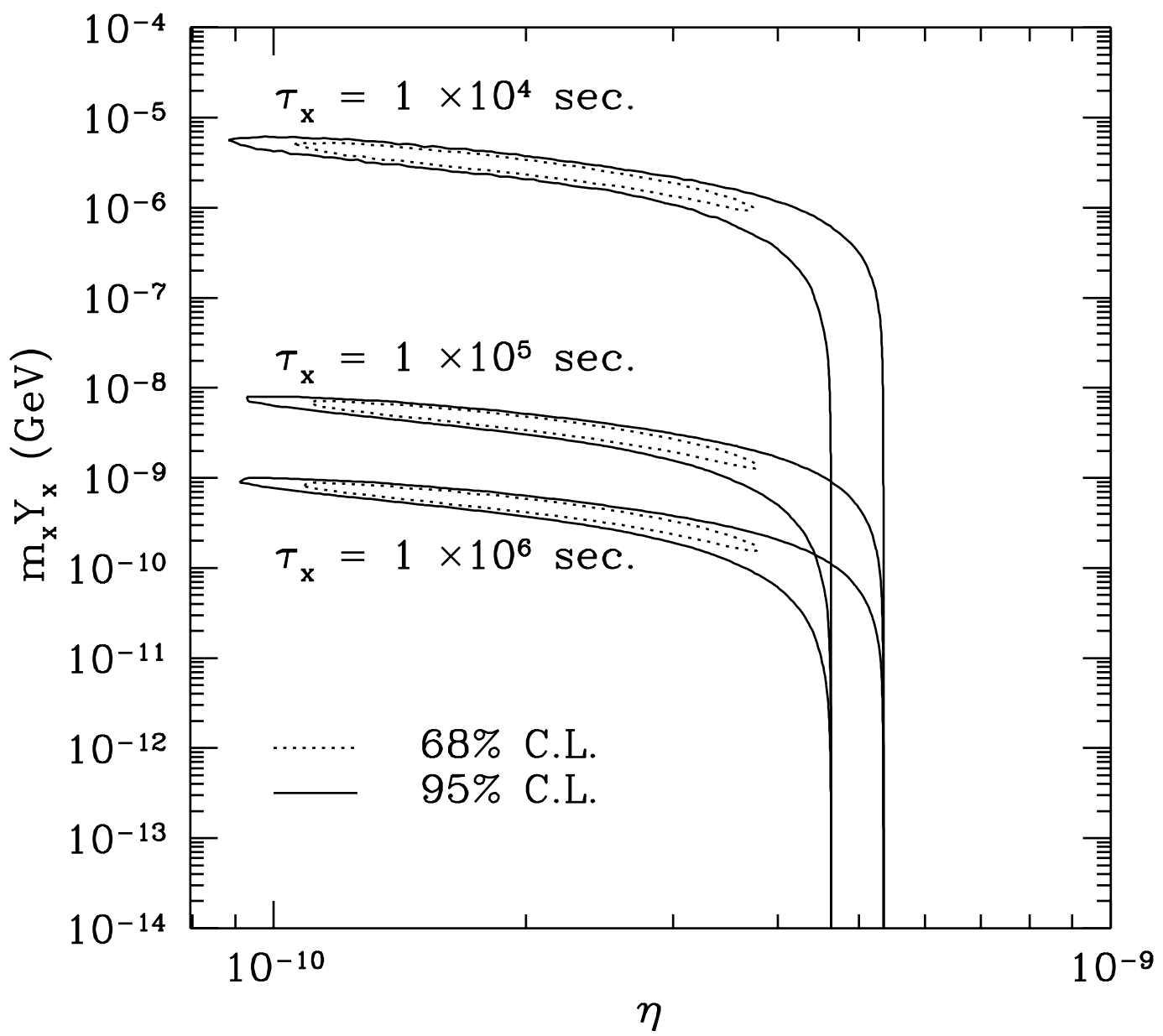
E. Holtmann et al. Fig. 7



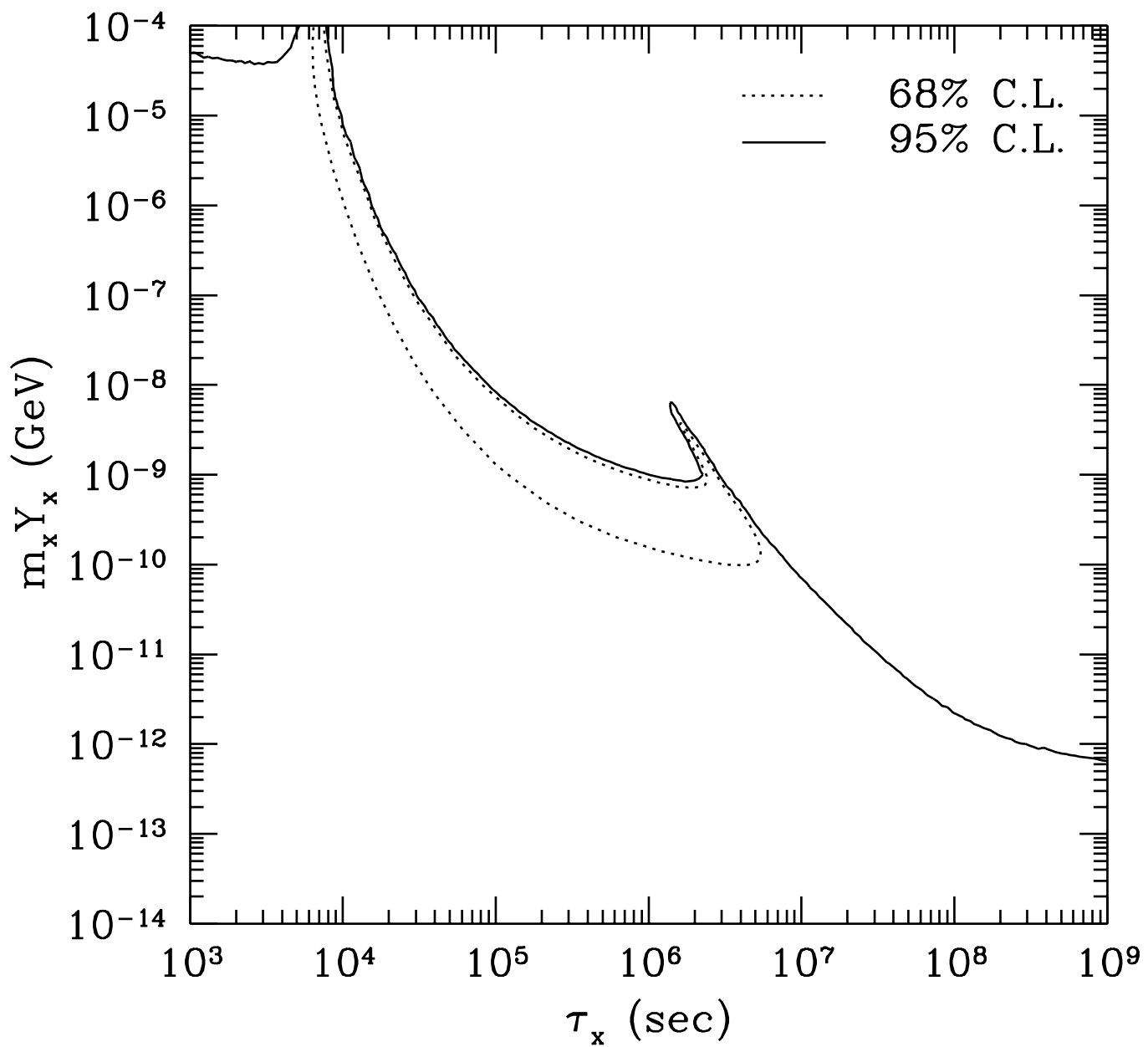
E. Holtmann et al. Fig. 8



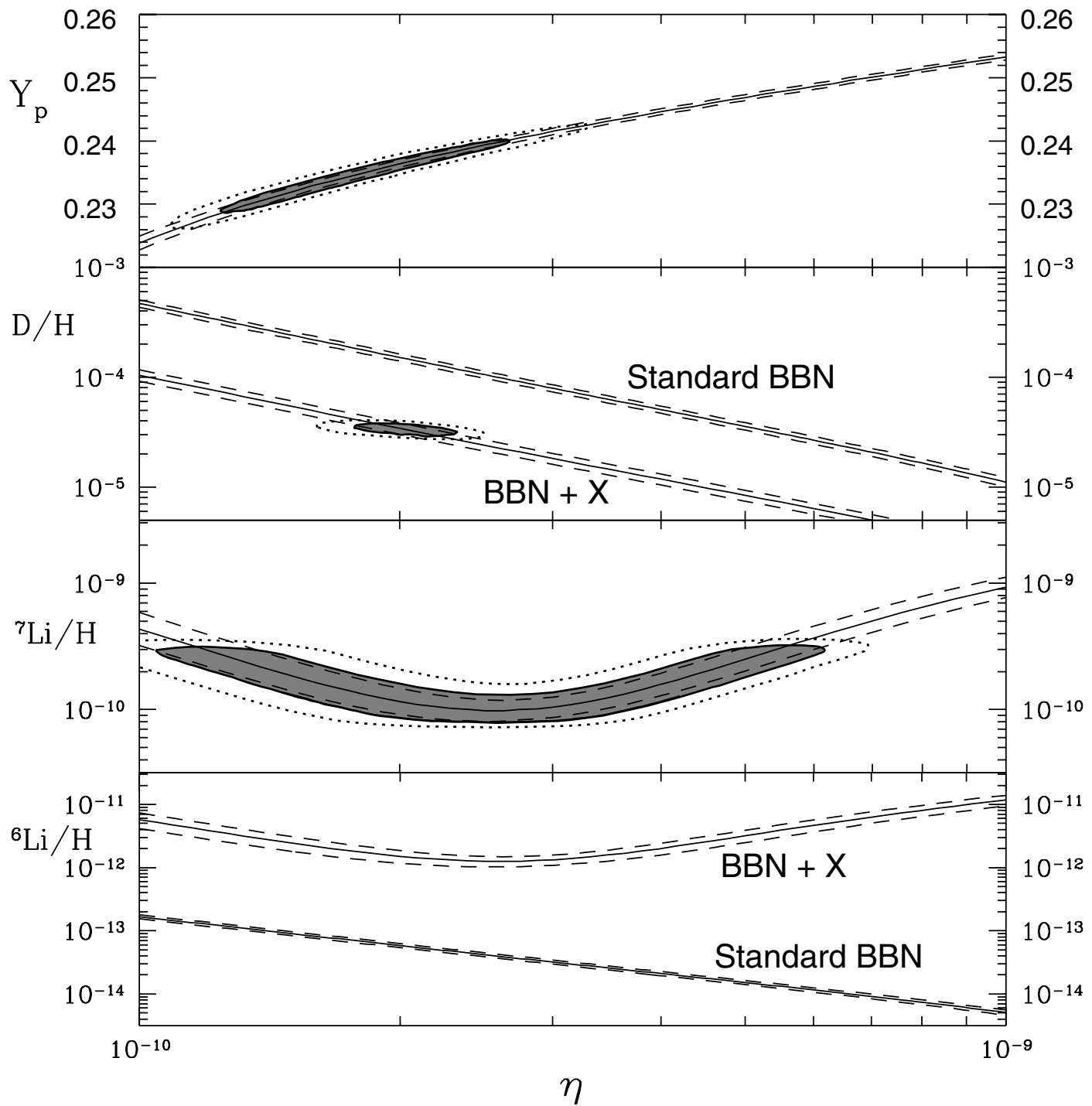
E. Holtmann et al. Fig. 9



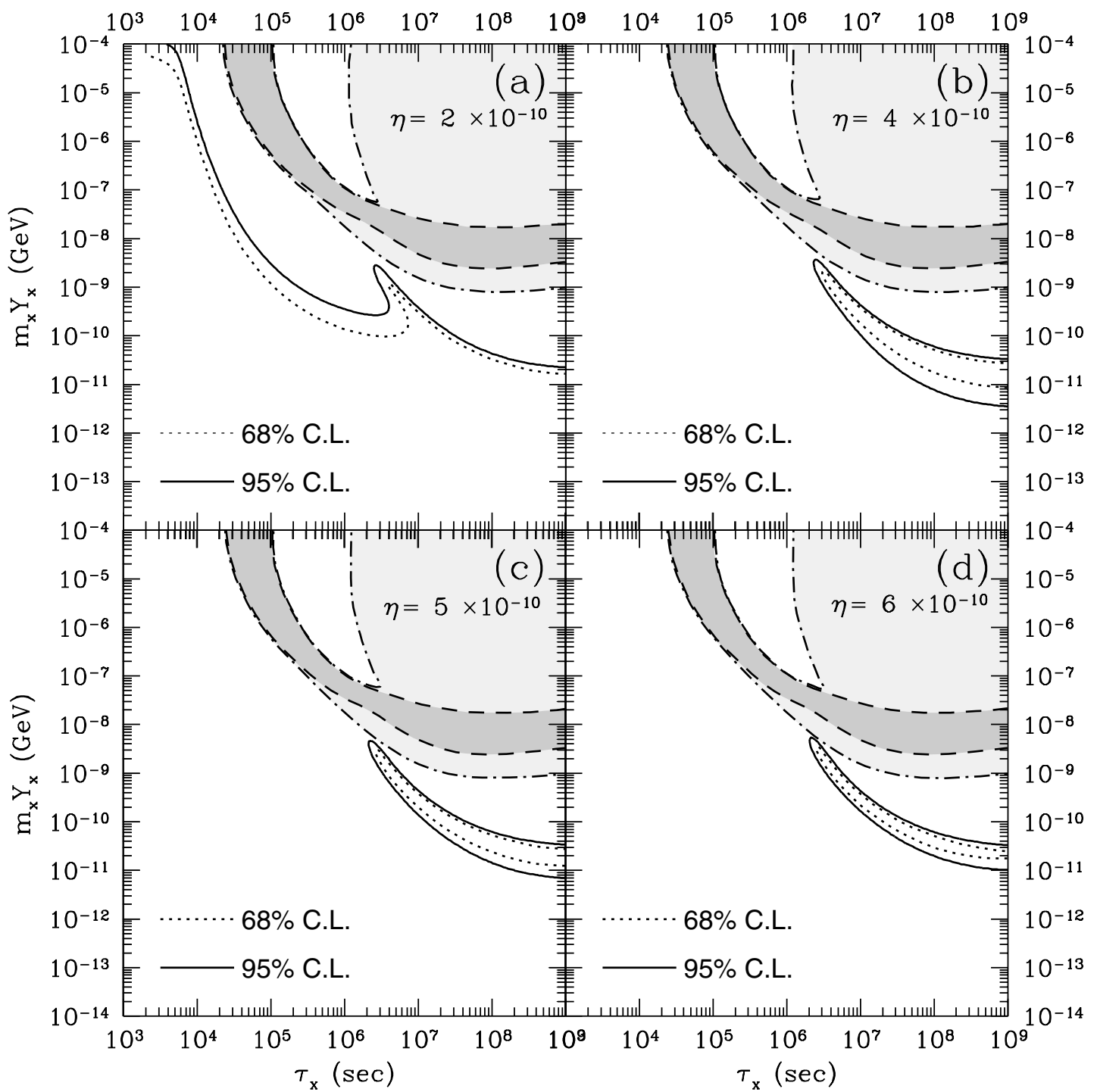
E. Holtmann et al. Fig. 10



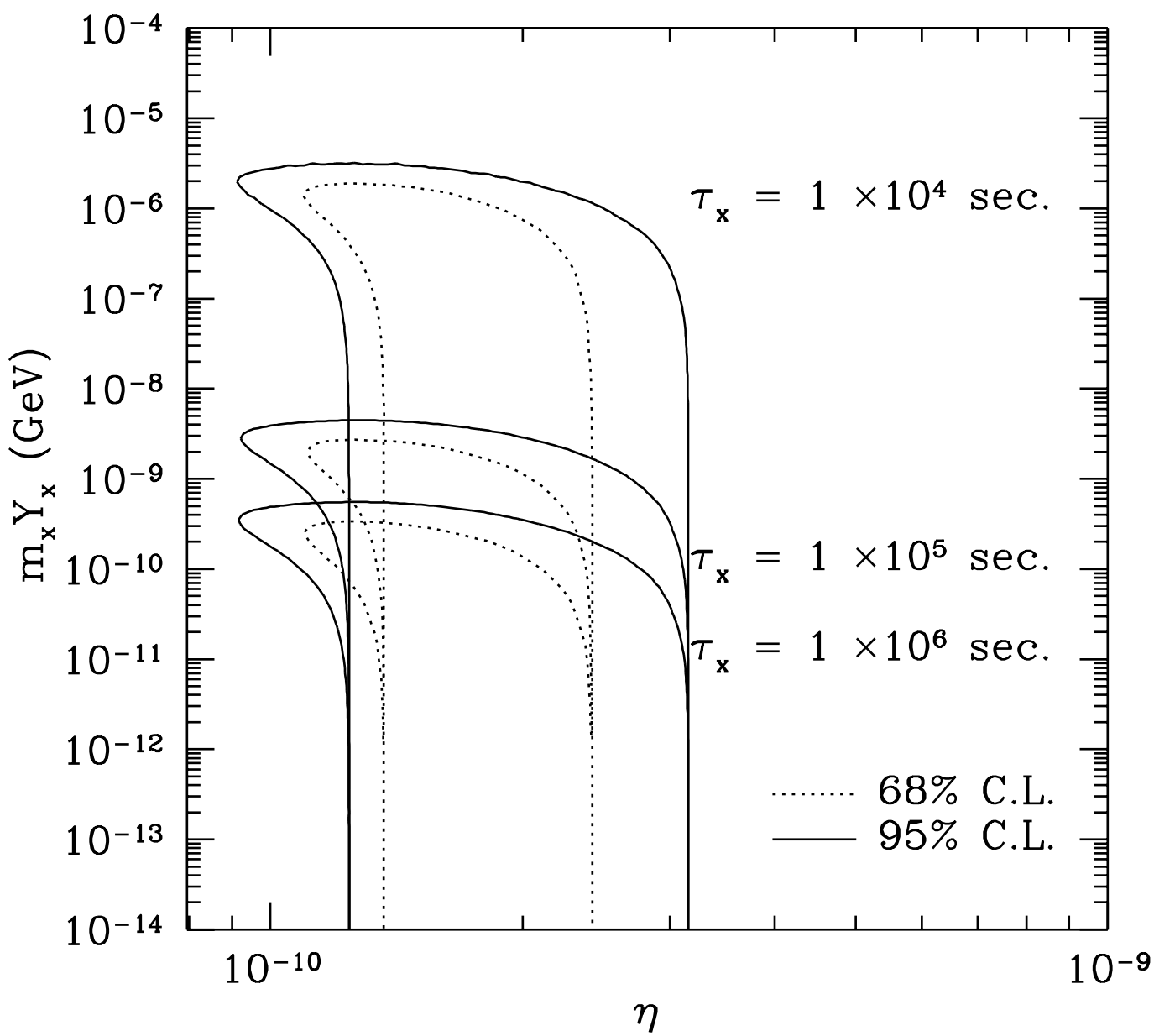
E. Holtmann et al. Fig. 11



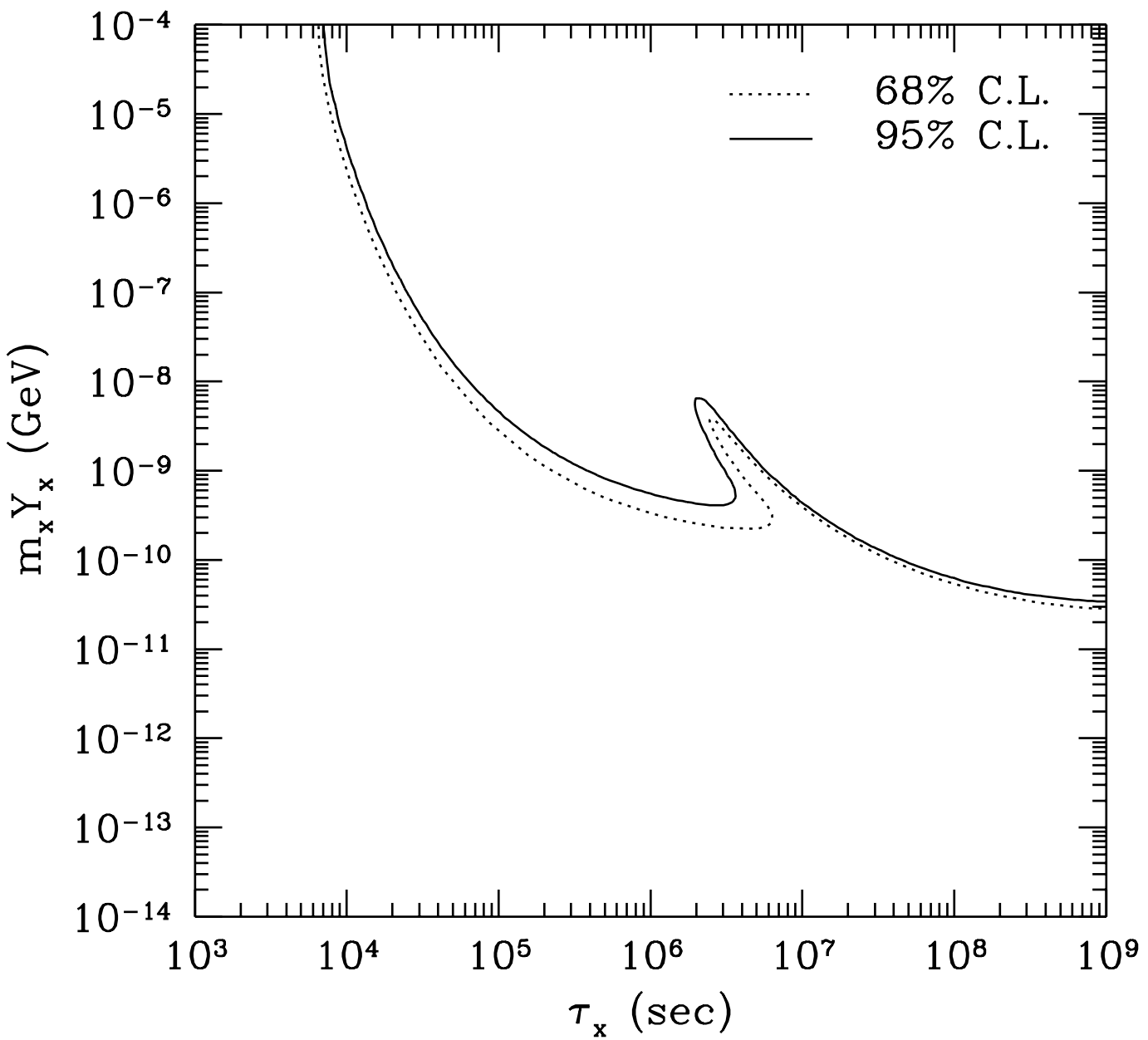
E. Holtmann et al. Fig. 12



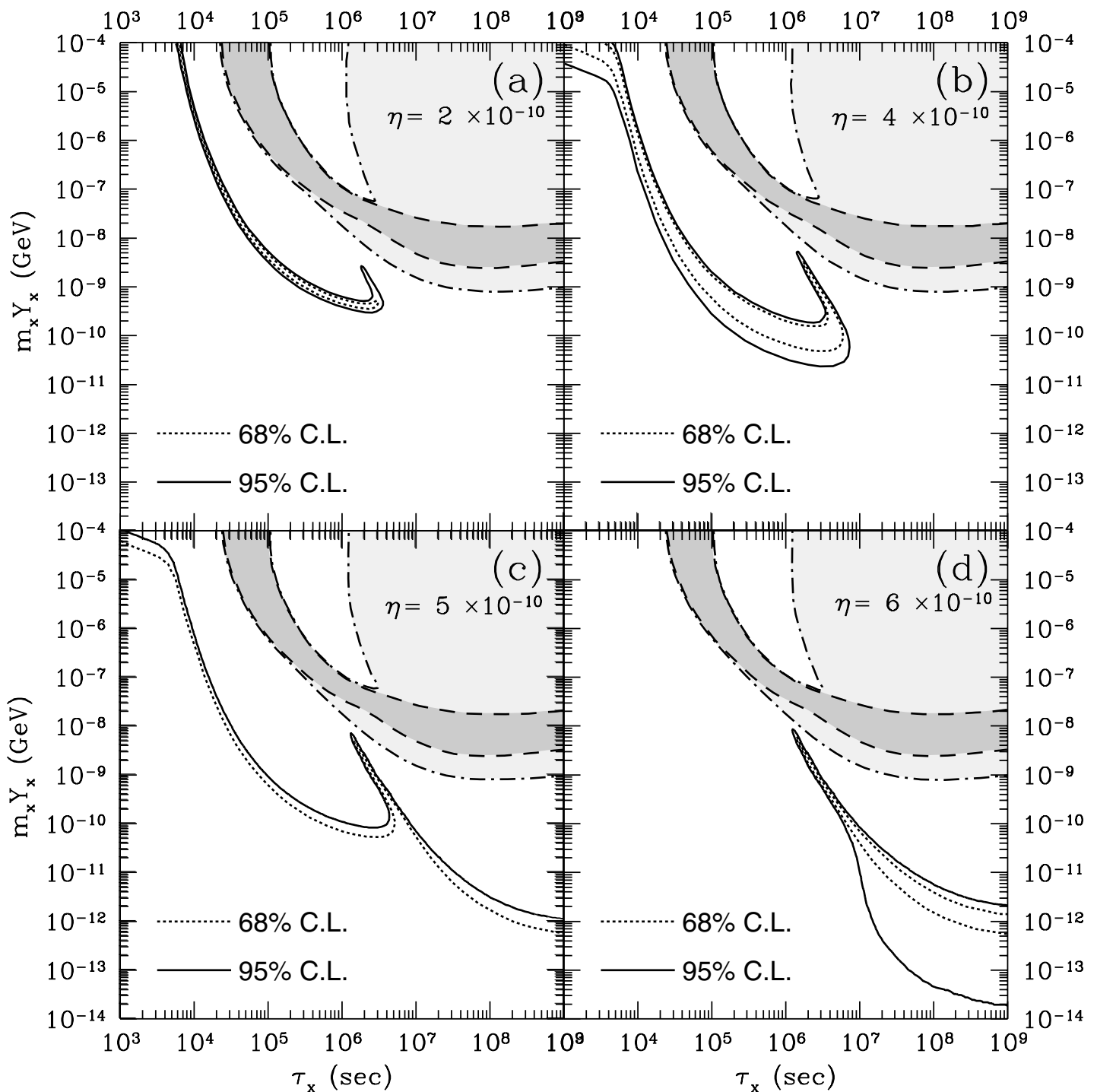
E. Holtmann et al. Fig. 13



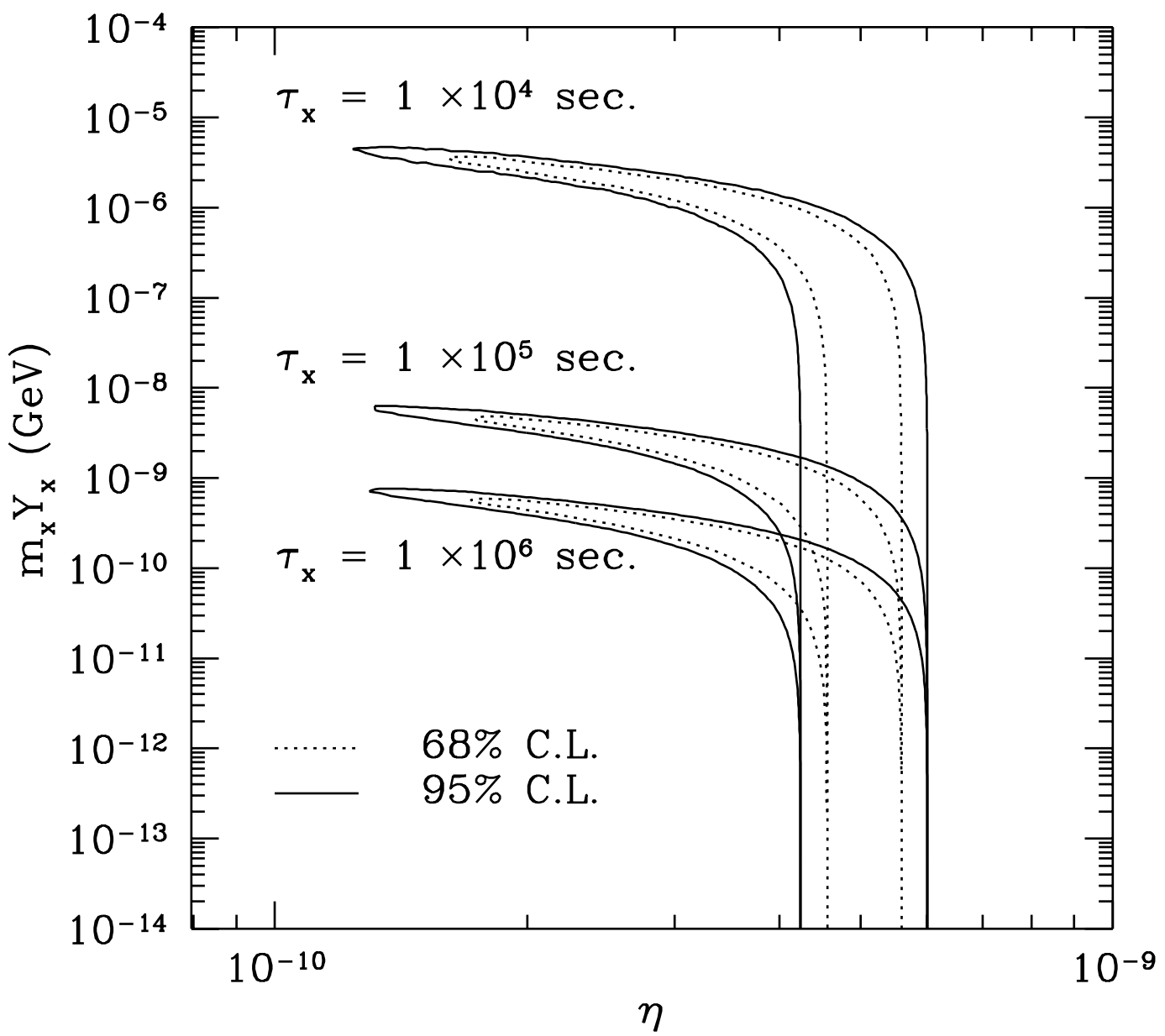
E. Holtmann et al. Fig. 14



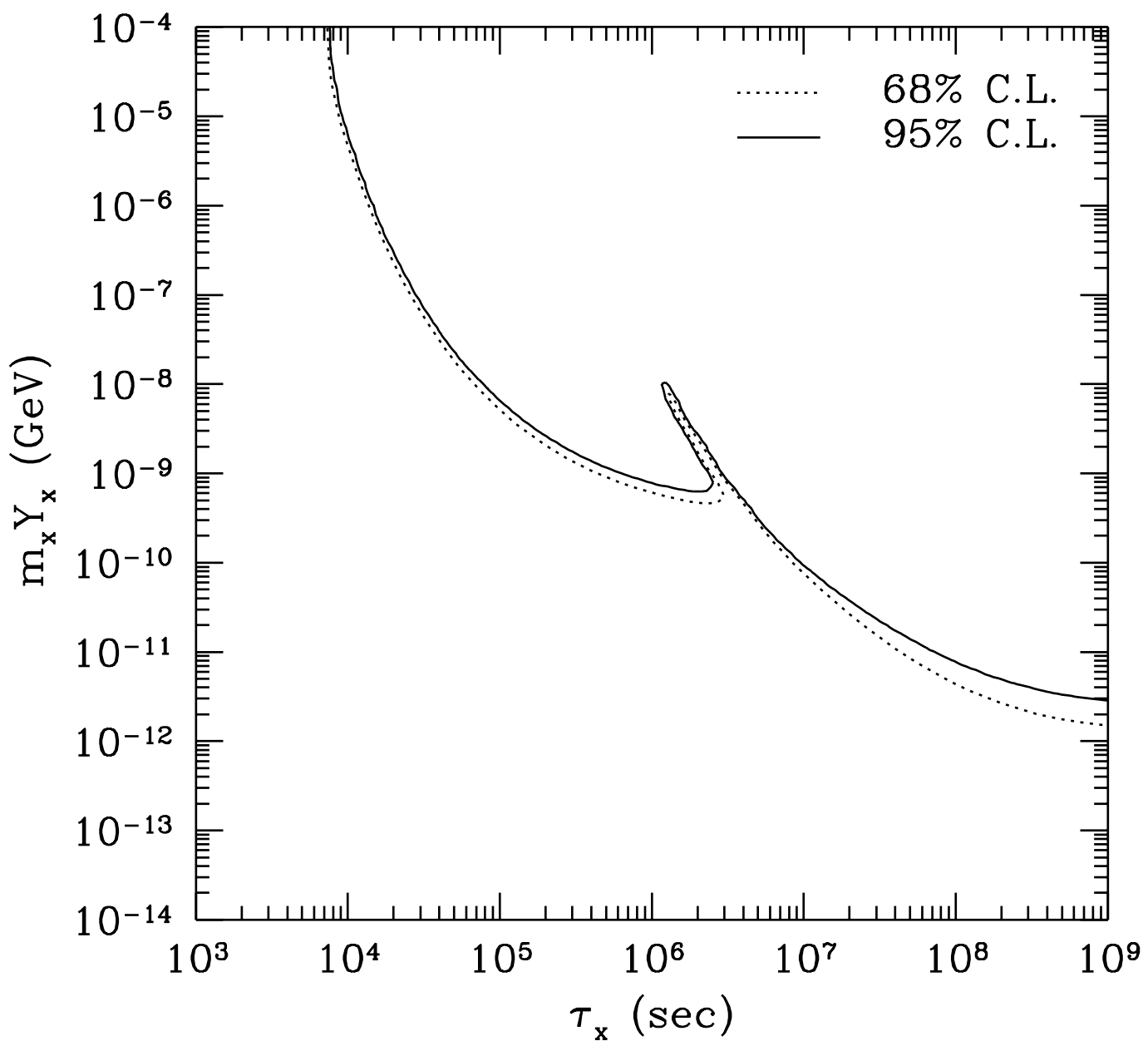
E. Holtmann et al. Fig. 15



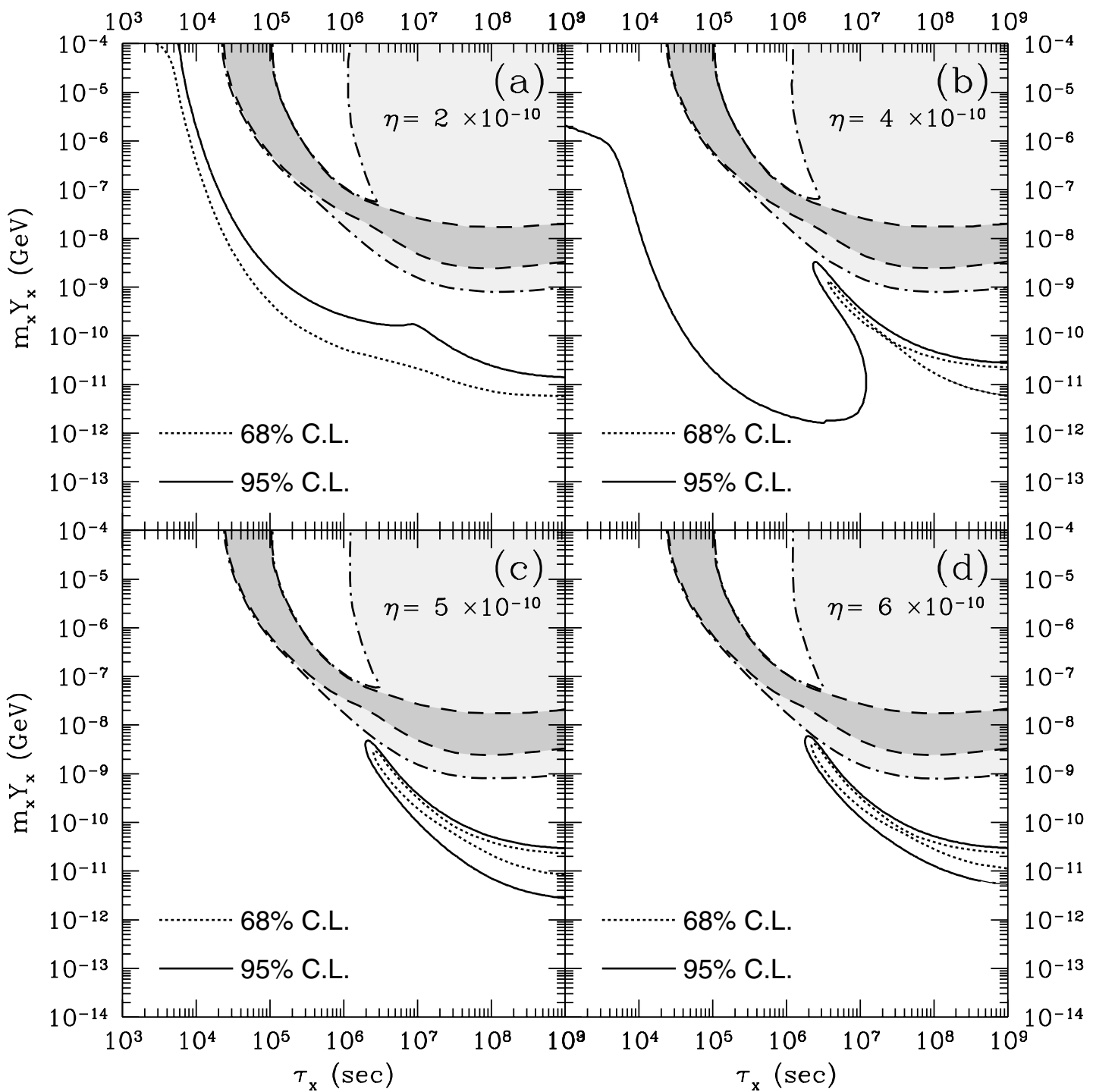
E. Holtmann et al. Fig. 16



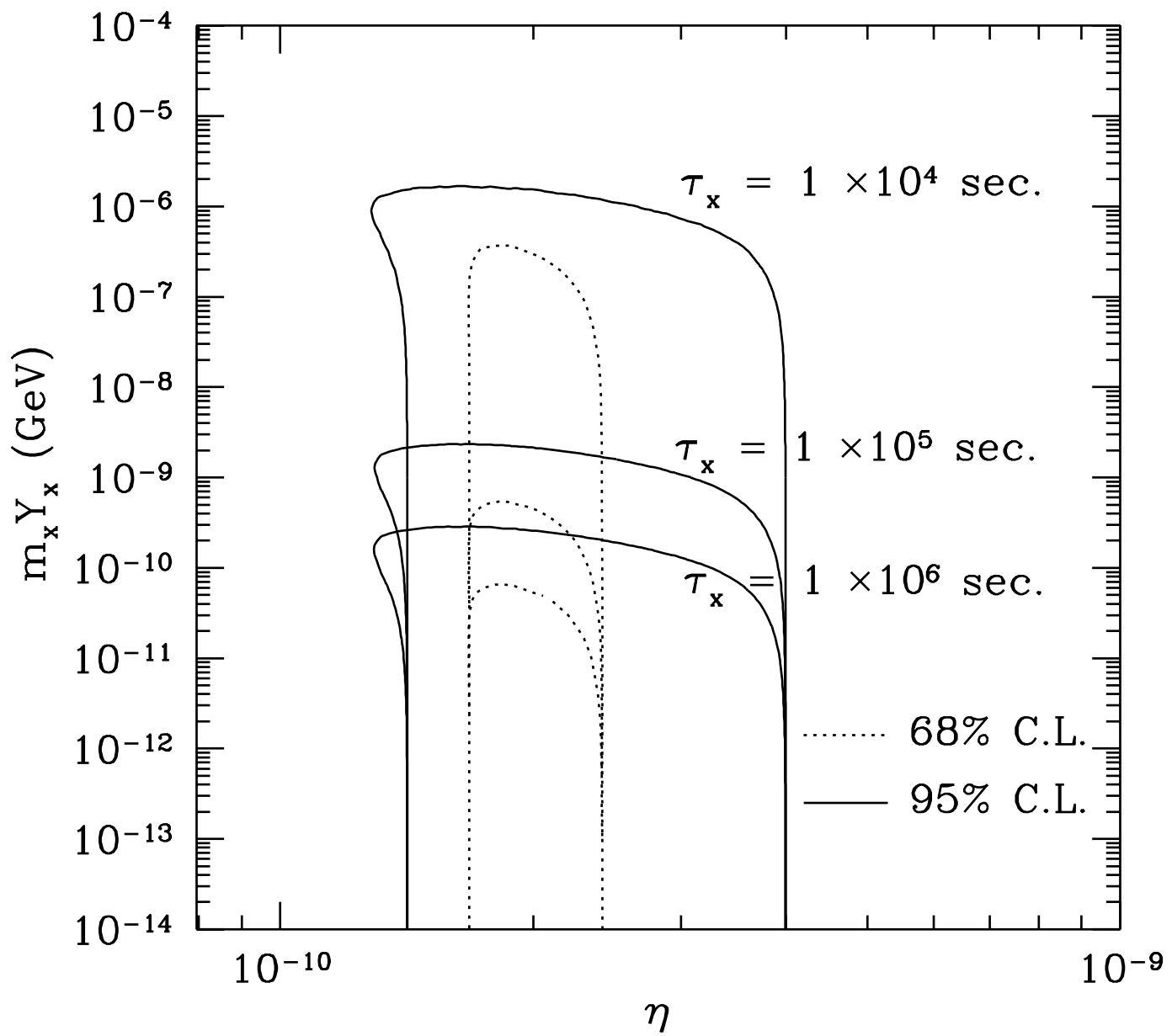
E. Holtmann et al. Fig. 17



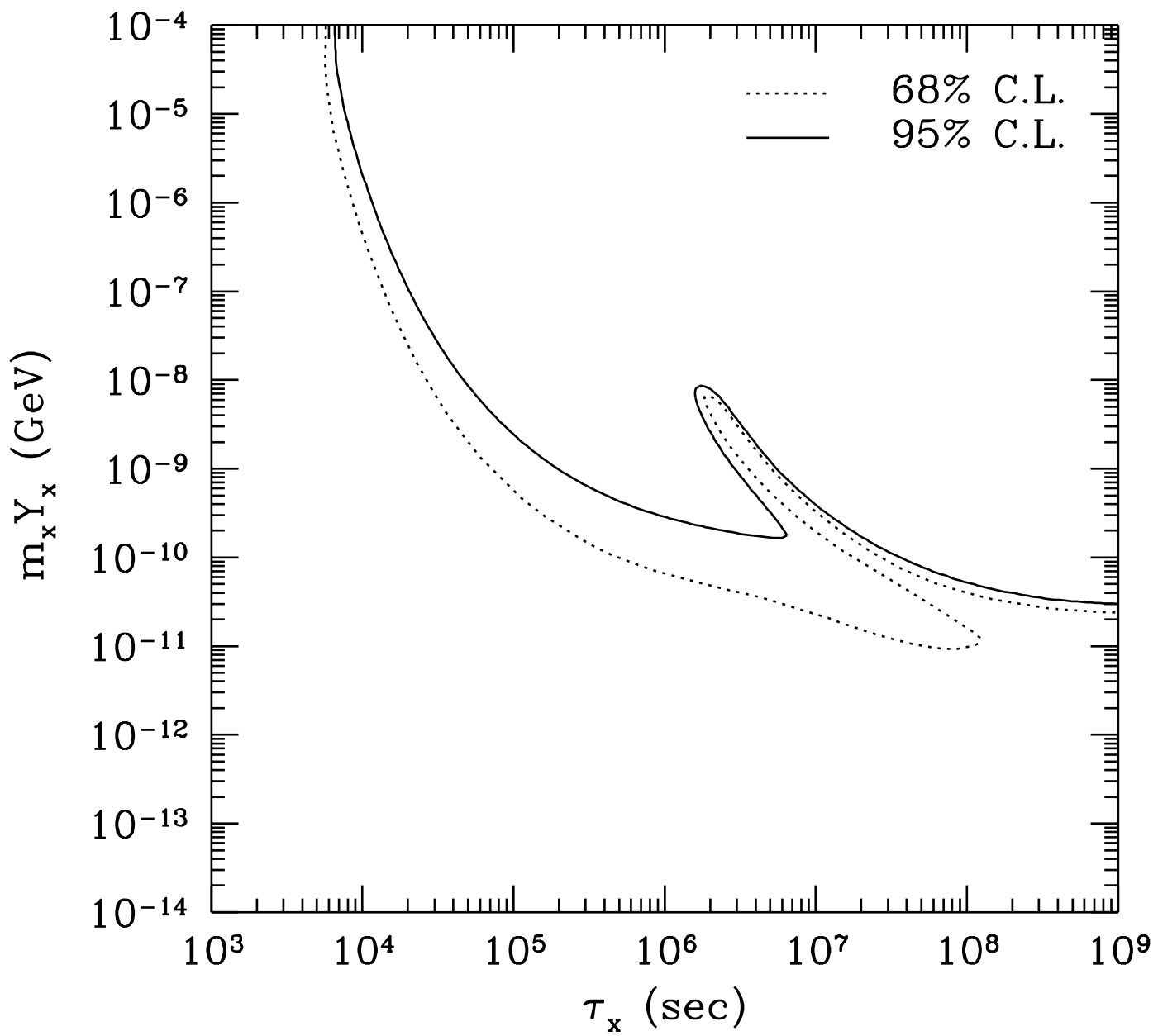
E. Holtmann et al. Fig. 18



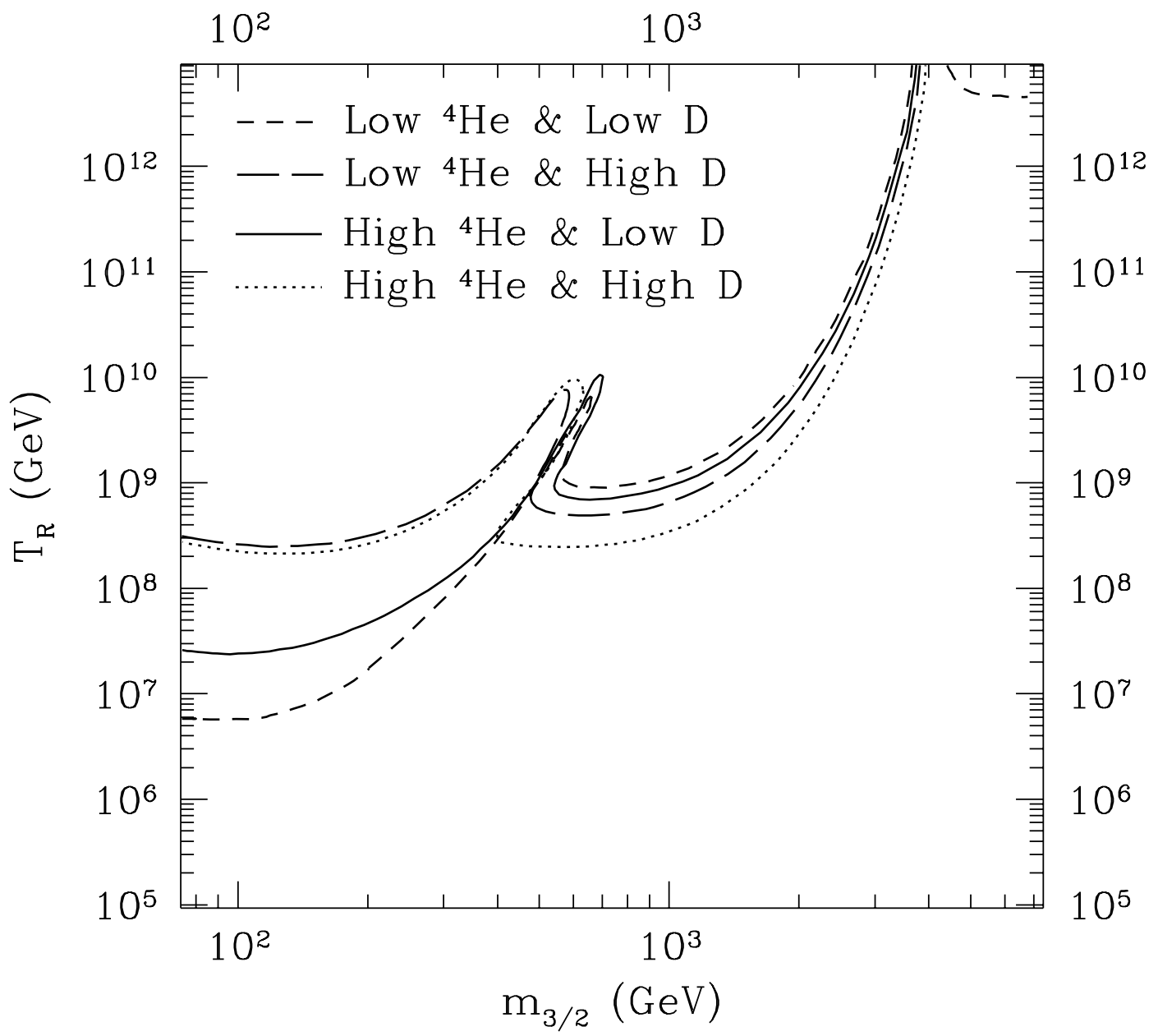
E. Holtmann et al. Fig. 19



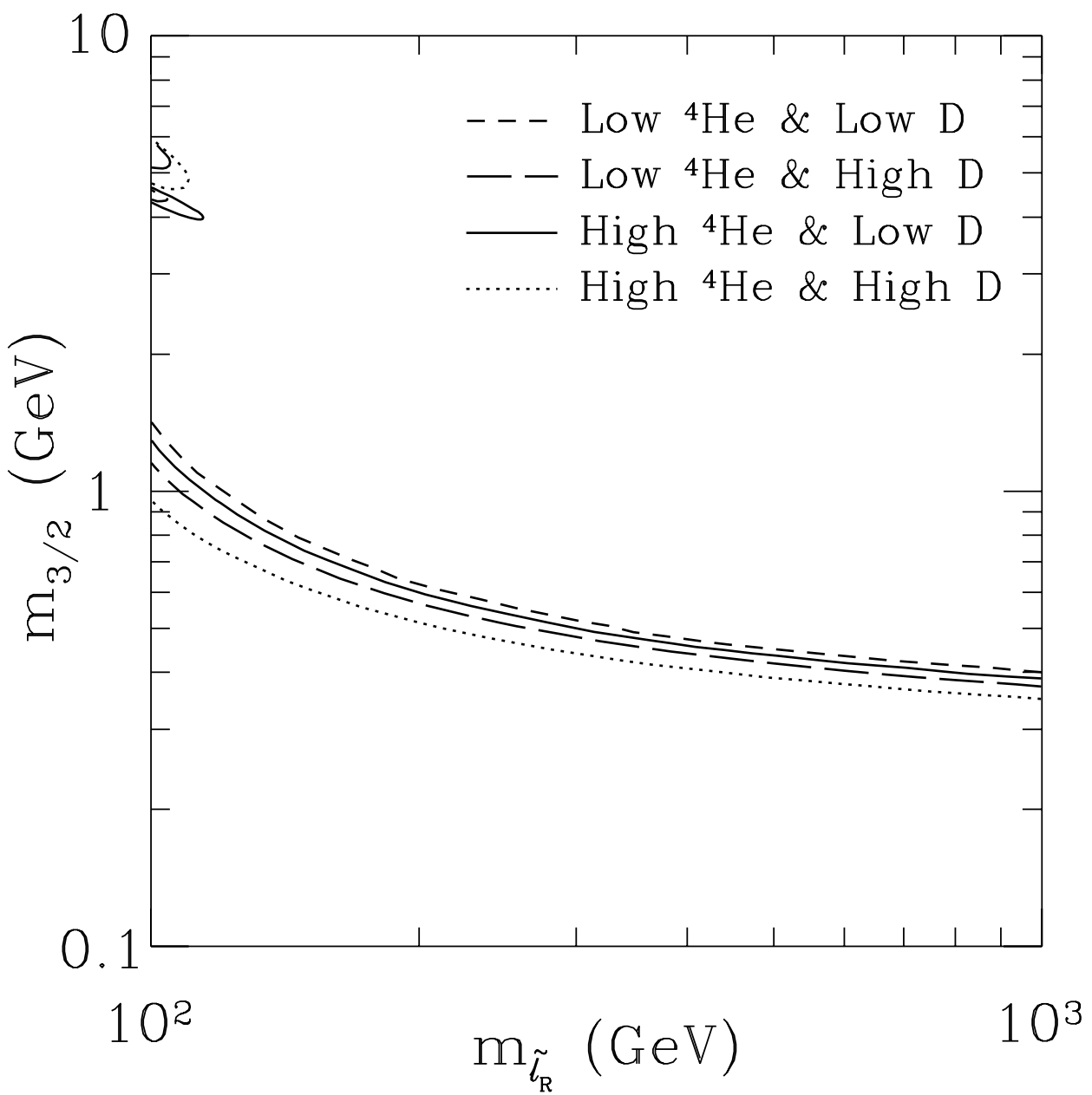
E. Holtmann et al. Fig. 20



E. Holtmann et al. Fig. 21



E. Holtmann et al. Fig. 22



E. Holtmann et al. Fig. 23